CHARACTERIZATION OF ISLAND-IN-THE-SEA BI-COMPONENT NYLON/ POLYETHYLENE TEREPHTHALATE FIBERS USING ATOMIC FORCE ACOUSTIC MICROSCOPY

A Thesis

Presented to the Faculty of the Graduate School

of Cornell University

in Partial Fulfillment of the Requirements for the Degree of

Master of Science

by

Soshana Adele Smith

August 2012

ABSTRACT

Within the last two decades, there has been growing interest in material properties at the nanoscale. The Atomic Force Acoustic Microscopy (AFAM) technique has been proven to be very useful for its ability to detect material properties at the nanoscale without sample damage. The following project has proven that the Atomic Force Acoustic Microscopy technique can be used on soft materials such as fibers. The nylon/ polyethylene terephthalate (PET) fibers were embedded in epoxy and microtomed in order to create a flat surface for imaging. The cross section of fibers was imaged using the AFAM technique. Information from the AFAM was then combined with mechanical beam theory in order to calculate the Young's modulus. The resulting measurements showed tip wear was not an influential force on the calculated Young's modulus results. On the other hand, changing the cantilever appears to have a great impact on calculated results. In regards to the fibers studied, the Young's modulus across the cross section of the fiber was discovered to be homogenous, with little changes seen from the center fibers to the peripheral fibers.

BIOGRAPHICAL SKETCH

Soshana Adele Smith was born in Kingston, Jamaica and grew up in Lauderhill, Fl. In 2005, she graduated from Boyd Anderson High School within the top 1% of her class. In 2009, she earned a B.S. in Chemical Engineering from Cornell University.

To my family and friends for all of their encouragement.

ACKNOWLEDGMENTS

I would first like to thank Professor Juan Hinestroza, my advisor and committee chairperson, for his direction, support and encouragement during my graduate career. From the beginning he has been a revolutionary force in my life. He has made me realize what potential I have and has been a great guide during the graduate process so far. I am also grateful to Professor Christopher Umbach, my minor committee member, who offered countless words of advice on this project.

I am extremely grateful for all of the technical support I received from John Grazul, Yuanming Zhang and John Hunt in the Cornell Center for Materials Research.

I would also like to thank all the faculty and staff members of the Department of Fibers Science & Apparel Design. In particular, I would like to thank Professor Margaret Frey for all her words of suggestions and words of encouragement, which were invaluable. I would also like to thank Professor S. Kay Obendorf, for being a great mentor and all her encouraging words. Additional thanks belong to my fellow group members especially Thomas Ellingham for always being available to discuss ideas and problems. I would also like to thank other graduate students within the Fiber Science Department such as Laura E. Lange, Eliza Allen, Sandy Flint, and Mark Chan for all their words of encouragement and support.

TABLE OF CONTENTS

LIST OF FIGURES

LIST OF TABLES

1. Introduction

Within the last few decades, the explosion of interest in nanoscale materials has led to the development of new techniques able to measure the properties of materials at various length scales. Among the new developments, Atomic Force Acoustic Microscopy (AFAM) technique has been garnering interest for its ability to provide nanoscale resolution of nanomechanical features within materials. Since its development approximately twenty years ago, it has been refined to make it an effective and reliable technique. However, AFAM has been used almost exclusively on stiff materials such as metals and thin films. In this thesis, we will use the AFAM technique to characterize, nylon/PET island-in-the-sea bicomponent fibers. The limitations and discrepancies of the AFAM technique and how those limitations can relate to the previous studies done on stiffer materials will also be discussed.

AFAM is a relatively new technique and so are the fibers being characterized. Bicomponent fibers have gained interest for their potential benefits derived from combining the properties of two polymers. Islands-in-the-sea are bicomponent fibers in which small fibers of one polymer are dispersed in the matrix of another polymer .The nylon, “island” fibers, will be main focus of the following research.

1.1 Objectives

The objectives of this project are two-fold. The first objective is to determine whether the AFAM technique is a reliable technique to be used in the characterization of polymer fibers. The second objective is to determine the elastic modulus of the bicomponent fibers.

2. Background

2.1 Atomic Force Microscopy (AFM)

The atomic force microscope(AFM)[1] was first introduced in 1986 by Gerd Binnig and Calvin Quate, as a way of overcoming the nanoscale resolution limitations of optical and scanning electron microscopes (SEM)[2]. An optical microscope is able to produce a flat 2D dimensional image of a sample surface, while a SEM requires a conductive surface in order to produce an image. The AFM, on the other hand, is able to overcome the limitations of both techniques, producing a three dimensional representation of a nonconductive surface.

An AFM uses a cantilever probe in contact/semi-contact with a surface in order to generate a map of a substrate's surface. A generic experiment begins by mounting a 100 - 350 nm cantilever, typically made from silicon or silicon nitride[3], on a piezoelectric actuator. Attached to the end of the underside of a standard AFM cantilever (Figure 1) is a sharp tip,

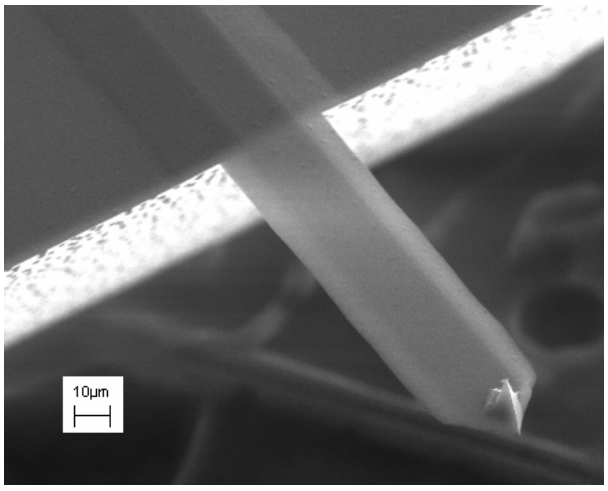

Figure 1 A typical AFM cantilever is made from silicon or silicon nitride. Depending on the stiffness of the cantilever, they range in length from 100 to 350 nanometers. Near the end of cantilever on the underside is a sharp tip.

which is able to sense nanoscale differences in height and material properties. Interactions between the cantilever tip and the sample cause deflections of the cantilever; to measure these deflections, a laser is reflected near the end of the cantilever onto a position-sensitive

photodetector consisting of two side-by-side photodiodes[4]. The difference between the dual photodiode signals is an indication of the position of the laser spot on the detector, hence providing the angular deflection of the cantilever.

AFM images can be acquired mainly in two ways, in tapping mode or contact mode. During contact mode, the tip is kept in constant contact with the sample and the deflection of the cantilever is maintained constant using a feedback system. Within the feedback system, the sensed deflection signal is sent to a DC feedback amplifier where it is compared to a set point. If the measured deflection is different from the desired value, i.e. the set point deflection, then the amplifier applies a voltage to the piezoelectric scanner to raise or lower the cantilever relative to the sample restoring the desired value of deflection. Contrary to contact mode, during tapping mode, the tip is only in contact with the sample approximately 50 percent of the time. At the beginning of a tapping mode experiment, the cantilever is being driven at a specific free oscillation amplitude. When the tip comes into contact with sample, a portion of the free oscillation amplitude will be dampened. The change in amplitude of the oscillation cantilever is detected by the photodetector and the signal is processed to give a topographical image of the sample surface.

2.2 Force Modulation

Force Modulation, an extension of the AFM technique in contact mode, quantitatively measures mechanical properties, such as surface elasticity[5]. As is typical during a contact mode scan, a Z-feedback loop maintains a constant deflection of the cantilever. A voltage usually between 1-5V is applied to either the tip or the sample, depending on the system, causing the cantilever or the sample to vibrate[6]. The force modulation image is a result of the variations in

the amplitude of the sample-tip vibrations. A hard sample surface offers greater resistance to the cantilever oscillation resulting in greater bending of the cantilever. While a soft surface will absorb the oscillation, deforming more under the applied force causing the amplitude response to be smaller. A schematic of the force modulation process can be seen in Figure 2. The force modulation technique can only provide a qualitative measure of differences in the properties of materials. The resulting force modulation image will only be able to show that there are two materials with different elasticity but the measurements would not be able to determine in a quantitative manner the actual elastic modulus values of the specimens.

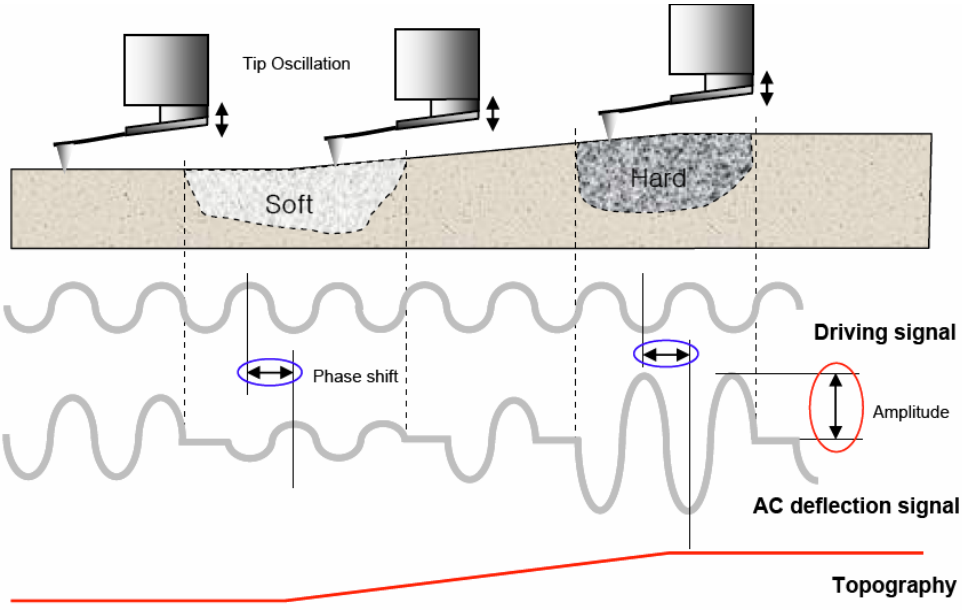

Figure 2 Schematic of the AFM force modulation mode.[7] Force modulation is a contact mode AFM technique, which requires the tip to be in contact with the sample at all times with a constant applied force. At the beginning of the experiment, a cantilever is also driven at a particular oscillation. When the cantilever comes into contact with materials of different elastic properties, the free oscillation of the cantilever is affected. With a harder sample, the oscillation of the cantilever will be deflected and the amplitude will be much larger than the free oscillation. Alternatively if the sample is soft, the sample will absorb some of the energy and the oscillation amplitude will be smaller.

2.3 Atomic Force Acoustic Microscopy (AFAM)

Atomic Force Acoustic Microscopy (AFAM) is an AFM mode that surpasses the limitations of force modulation by determining the local contact stiffness, which can then be used to determine the Young's modulus of the specimen[8,9]. At the beginning of an AFAM experiment the sample under investigation is fixed to a longitudinal ultrasonic transducer. A schematic of the AFAM set-up can be seen in Figure 3. A computer-driven function generator drives the transducer, exciting the sample, and causing it to vibrate. The vibration of the surface produces flexural vibrations on the cantilever, whose tip is always in contact with the sample surface. The oscillation of the cantilever causes the laser, which is being reflected off the backside of the cantilever, to deflect. These deflections are picked up by a position sensitive four-section photo-diode and the resulting signal is transferred to a lock-in amplifier, registering the amplitude of the cantilever vibration. Upon sweeping the driving frequency of the cantilever the values for contact resonance frequencies, f_n, are obtained.

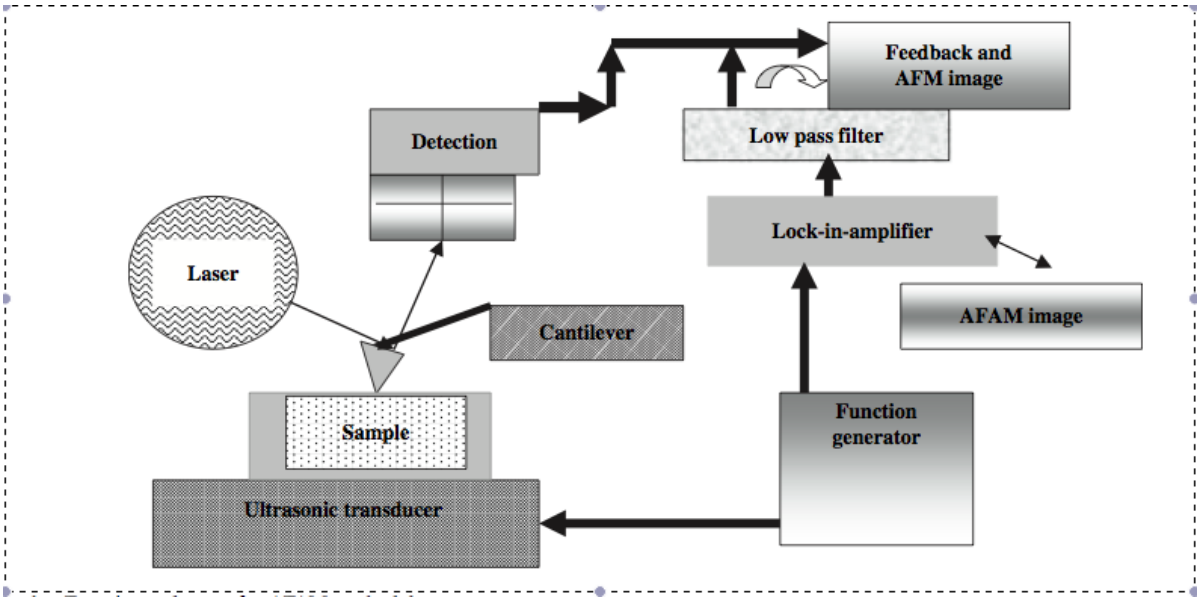

Figure 3 Experimental set- up of AFAM[10] A sample is placed on top of an ultrasonic transducer which is driven by a computerized function generator. The sample is also excited as a result of the continuous sine waves from the driven transducer. Depending on the stiffness of the material, various resonances of the cantilever are possible causing it to oscillate at various amplitudes. The cantilever vibrations are measured by 4-sectioned photo-diode and evaluated by lock in amplifier.

When the contact stiffness, k^*, between a tip and a sample surface is high, the resonance curve will shift towards a higher frequency and it is an indication of a hard sample. The opposite is true as well; with a soft sample causing a shift to the left, to lower frequencies. Banarjee *et al.*[35] explained this in detail as illustrated in Figure 4. The fixed end of a cantilever has one node of vibration at a fixed position on the substrate. The position of the other node depends on the rigidity of the sample surface. In the softer region, the node is deeper into the sample and in the harder region, the node is closer to the sample's surface. When the tip is in contact with the softer region, the wavelength of the cantilever vibration, λ_s, will increase. This behavior results in a decrease of the cantilever's vibrational frequency, f_s. As a result, as the tip moves from a harder region to a softer region, the frequency of vibration decreases.

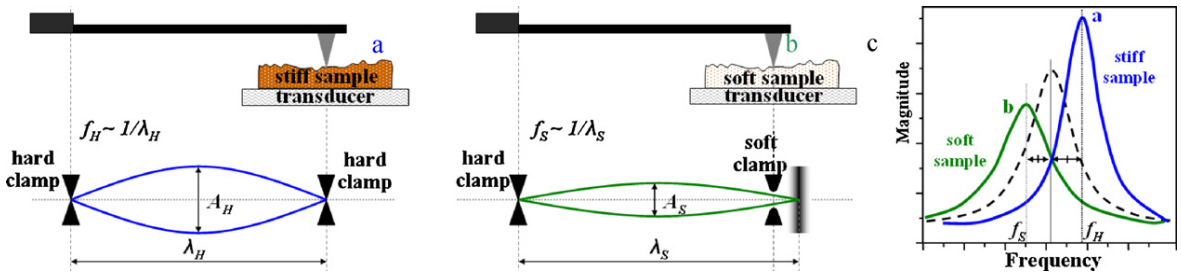

Figure 4 - Schematic representation of cantilever vibration when tip is in contact with a hard and a soft surface. Here, f is the cantilever's vibrational frequency and λ is the wavelength of the cantilever vibration, and *h* and *s* stand for hard and soft respectively[11].

2.3.1 AFAM Theory

Once the AFAM experiment is complete and vibrational frequencies are collected, a series of mechanical theories are used in order to obtain the Young's modulus of the specimen. First, the contact stiffness is determined using theory of beam oscillations. The contact stiffness is then related to the elastic modulus using a contact theory to model the interaction between the cantilever tip and the sample.

AFM cantilevers are modeled as analogous to clamped beams vibrating in different modes, such as flexural, torsional, and extensional.[12] Analysis of the torsional and flexural vibration modes result in closed form solutions of equations of motion for vibrating beams[13,14]. For a beam with a uniform rectangular cross section, the equation of flexural motion is the fourth order differential seen in Equation (1) if damping is neglected[15].

$$EI\frac{\partial^4 y(x,t)}{\partial x^4} + \rho A\frac{\partial^2 y(x,t)}{\partial t^2} = 0 \qquad (1)$$

In Equation (1), E is defined as the Young's modulus (GPa), ρ (kg/m^3) is the density of the cantilever material, $A = W{\cdot}T$ (m) is the cross section of the beam and I (kg·m²) is the area moment of inertia. W and T are, respectively, the width and the thickness of the cantilever. For a

beam with a rectangular cross section, $I = WT^3/12$, x is the coordinate in the longitudinal direction parallel to the probe. Additionally, $y(x)$ is the deflection of the beam from the equilibrium position.

To begin to solve equation (1), it is best to first separate the $y(x,t)$ in Equation (1) into time and space components[16]. When this is done by restating $y(x,t) = Y(x)\,F(t)$ Equation (1) becomes:

$$EI\frac{\partial^4 \mathrm{Y(x)F(t)}}{\partial x^4} + \rho A\frac{\partial^2 \mathrm{Y(x)F(t)}}{\partial t^2} = 0 \tag{2}$$

Using the separation of variables method and rearranging equation (2), we obtain the following equation:

$$\frac{EI}{pA\,Y(x)}\frac{\partial^4 \mathrm{Y(x)}}{\partial x^4} = \frac{-1}{f(t)}\frac{\partial^2 \mathrm{F(t)}}{\partial t^2} \tag{3}$$

In order for both sides of Equation (3) to equal, they both must equal the same positive constant, which is denoted in this case by ω^2, where $\omega = 2\pi f$. Rearranging and ignoring the time dependence on the right, (Equation 3) is reduced to (Equation 4 and Equation 5).

$$\frac{EI}{pA}\frac{d^4 \mathrm{Y(x)}}{dx^4} = \omega^2 Y(x) \tag{4}$$

$$\frac{\partial^4 \mathrm{Y(x)}}{\partial x^4} - {k_n}^4\, Y(x) \tag{5}$$

where

$${k_n}^4 = \frac{\rho A}{EI}\omega^2. \tag{6}$$

The general solution for (5) will be

$$Y(x) = A\,\sin k_n x + B\cos k_n x + C\sinh k_n x + D\cosh k_n x = 0 \tag{7}$$

In order to solve (7), four boundary conditions are needed[17]. If the cantilever is modeled as a clamped-spring end beam (Figure 1), then the following boundary conditions can be developed:

- At $x=0$

$$Y(0,t) = 0 \tag{8}$$

$$\frac{dY(0,t)}{dx} = 0 \tag{9}$$

- At $x=L$

$$\frac{d^2Y(L,t)}{dx^2} = 0 \tag{10}$$

$$\frac{d^3Y(L,t)}{dx^3} = \frac{3k^*}{k_c{L_1}^3} \tag{11}$$

At the clamped end, $x = 0$, there is no deflection and hence the slope of deflection is zero.

$$Y(0,t) = 0 \tag{8}$$

$$\frac{dY(0,t)}{dx} = 0 \tag{9}$$

When the tip comes into contact with the sample's surface, the tip-sample interaction is modeled as a spring coupled beam, assuming there are only same vibration amplitudes. The boundary condition is as follows: At $x = L$, the beam does not bend, so there is an assumption of no transfer of moment, therefore Equation (10)[18] is achieved.

$$\frac{d^2Y(L,t)}{dx^2} = 0 \tag{10}$$

The last boundary condition is the result of the shear the shear force between the cantilever and the sample when they are in contact. The tip senses long-range attractive forces as well as repulsive tip–sample forces. The applied load felt by the sample, P, can be expressed as $P = k_c\, x\, d_c$[19]; Where d_c is the cantilever deflection and k_c is the spring constant. The equation for k_c seen in equation (11) makes the assumption that the cantilever has a rectangular cross section with width, W, thickness, T and length, L[20].

$$k_c = \frac{EWT^3}{4{L_1}^3} \tag{11}$$

If the tip-sample vibration amplitudes are kept small then the interaction can be modeled as linear[21] with a spring constant k^*, which is the negative derivative of the tip-sample force in the equilibrium position:

$$k^* = -\frac{\partial F(z)}{\partial z} \tag{12}$$

where z is the tip-sample distance, $F(z)$ if the tip-sample force. Using this relation the fourth boundary condition becomes

$$EI\frac{d^3Y(L,t)}{dx^3} = k^*Y(x) \tag{13}$$

which combined with (Equation 11) yields (Equation14).

$$\frac{d^3Y(L,t)}{dx^3} = \frac{3k^*}{k_c{L_1}^3} \tag{11}$$

Applying the first boundary condition (Equation 8) yields $B + D = 0$, whereas the second boundary condition (Equation (9) yields $A + C = 0$. The general solution can then be temporarily written as:

$$Y(x) = A\ \sin k_n x - B\cos k_n x\ + A\sinh k_n x - B\cosh k_n x = 0 \tag{14}$$

Applying the third boundary condition (Equation 10) yields $A = B\gamma$, where the constant, γ, is defined as

$$\gamma = \frac{\cosh k_n L + \cos k_n L}{\sinh k_n L + \sin k_n L} \tag{15}$$

The general equation now has the form seen in Equation (16).

$$Y(x) = -B\gamma \sin k_n x - B\cos k_n x - B\gamma \sinh k_n x - B\cosh k_n x = 0 \tag{16}$$

Evaluation of equation (14) yields equation (17) as seen below.

$$\frac{d^3 Y(L,t)}{dx^3} = B\gamma \cos k_n L + B\sin k_n L + B\gamma \cosh k_n L - B\sinh k_n L = 0 \tag{17}$$

Pulling in equation (16) and equation (17) into equation (13) yields

$$k^* = \frac{k_c L^3(\cos k_n L \cosh k_n L + 1)}{3(\cos k_n L \sin k_n L - \cosh k_n L \sin k_n L)} \tag{18}$$

Equation (19) can be written explicitly in terms of the resonance frequency through rearrangement.

$$k^* = \frac{k_c(c_c\sqrt{f})^3(1 + \cos c_c\sqrt{f} \cosh c_c\sqrt{f})}{3\left(\cos c_c\sqrt{f} \sin c_c\sqrt{f} - \cosh c_c\sqrt{f} \sin c_c\sqrt{f}\right)} \tag{19}$$

where

$$c_c = L\sqrt[2]{2\pi}\sqrt[4]{\frac{\rho A}{EI}} \tag{20}$$

Once the contact stiffness is obtained, a contact model is needed to relate the contact stiffness to material properties, such as elastic modulus. At the time when two non-conforming solids are brought into contact, they will have contact at a point or along a line.[22] Under the

initiation of the slightest load, the area of contact will increase. A contact theory is then needed to analyze and predict the area of contact and how it varies with applied load.

Over the last 150 years there have been various theories that have been put forth to model the interactions between solids in contact. The first theory was developed by Heinrich Hertz in 1822 while studying Newton's optical inference fringes in the gap between two lenses. During the course of his study, he became interested in the possible influence of plastic deformation between the two surfaces. Hertz made a few assumptions[22]:

i) Each body is to be regarded as an elastic half space loaded over a small elliptical region of its plane surface;

ii) Dimensions of the contact area are required to be significantly smaller than that of dimensions of each body and the relative radii of curvature of the surfaces;

iii) Applied strains are small;

iv) Surfaces are assumed to be frictionless so only a normal pressure is transmitted between them[23].

If the tip is modeled as a sphere, the sample modeled as free space and adhesive forces ignored, then the Hertzian equation can be used in the form seen in equation (22).

$$k^* = \sqrt[3]{6\,E^{*2}RF_0} \tag{21}$$

Where E^* is the effective Young's modulus of the tip-sample contact, R is the radius of curvature of the tip and F_0 (N) is the applied load. All variables in Equation (22) are known except for the effective Young's modulus, therefore Equation (22) can be re-arranged into the following form:

$$E^* = \sqrt{\frac{k^{*3}}{6RF_0}} \tag{22}$$

The effective Young's modulus can be written as a combination of the sample and tip's Young's moduli, E_t and E_s, and Poisson ratio, ν_t and ν_s.

$$\frac{1}{E^*} = \frac{1 - {v_t}^2}{E_t} + \frac{1 - {v_s}^2}{E_s} \tag{23}$$

Most AFM tips are made from silicon Young's modulus and Poisson ratio of silicon are known to be in the proximity of 169 GPa and 0.33 respectively.

2.3.2 Previous Applications of the AFAM Technique – Metals

When the AFAM theory was first developed it was tested mostly on stiff substrates such as ferritic metals, silicon and aluminum. In 2000, Rabe *et al.* published a study investigating the capabilities of the AFAM technique on various materials[9]. They first investigated a correlation between oxidation time of nanocrystalline ferrite thin films and its effect on Young's modulus. The results showed an overall decrease in the Young's modulus with increasing oxidation time, hence confirming the hypothesis of a chemical gradient in the nanocrystalline material due to the oxidation. However there were large variations in the data as high as 100% and as low as 20%. These variations were explained by a high lateral resolution, given by the contact area formed by the AFM tip and the surface. At the nanoscale, parts of a sample can be very different. The AFAM technique is able to detect these nanoscale differences that result in the large variations in the values being measured. Though not discussed in their paper, a few other issues and assumptions may also have accounted for the wide variations seen in that study. For example, the Poisson ratio was assumed to remain the same, 0.30, for all samples even after oxidation; this may not be accurate. In addition, further deviations from the theoretically anticipated values may be attributed to the fact that the dimensions of the cantilever were not directly measured. Deviations resulting from the dimensions of the cantilever can have a great impact on

determining the spring constant of the cantilever. This in turn will affect your constant stiffness and hence the reported magnitude of the Young's modulus. Evidence of this can be seen in a paper written by *Kim et al.*[24] in which the spring constant calculated using tip dimensions yielded $k_c = 0.087$ N/m, was almost twice the value provided by the manufacturer, $k_c = 0.041$ N/m. Similarly Marinello *et al.*[25] also proved that the actual difference in spring constant between tips from the same batch can be between than 10–20% or even higher. In the years following the publications of this work, many began to focus on the assumptions and factors that affect AFAM measurements.

In 2002, *Rabe et. al*[26] compared the AFAM technique to other ultrasonic microcopy techniques, most notably ultrasonic piezoelectric force microscopy. As seen in Figure 5, AFAM provided a vast improvement over AFM by showing the greatest contrast and surface details. Following the topographical experiments, an indentation modulus measurement of the $BaTiO_3$ piezoelectric sample was performed in order to test the preciseness of the AFAM technique. Using silicon and a SrTiO3 crystal as the reference materials, the following data was reported: the a-domain material had an indentation modulus of 318 ± 30 GPa, while the c-domain materials were 220 ± 50 GPa. These values had a 40 percent variation when compared to the reported values of 213 GPa and 155 GPa[27]. This notable variation was explained by the elastic properties of BaTiO3 single crystals being dependent on the method of crystal preparation. The authors could not state with certainty that their material was prepared in an identical manner to that of the crystals in literature[28].

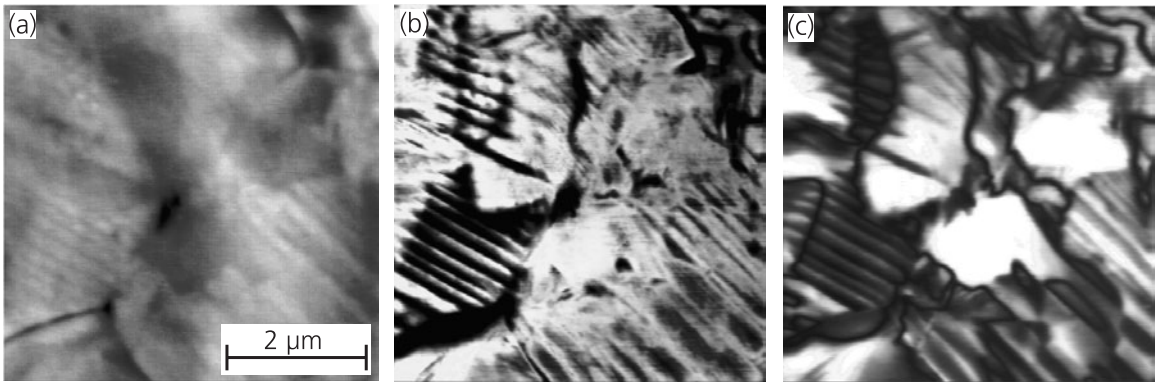

Figure 5 Comparison between three 5 × 5 µm^2 of the same surface area of a PZT ceramic surface; *(a)* topography, (*b*) AFAM and (*c*) ultrasonic piezo-mode images. The AFAM image delivered the greatest contrast and details between the two piezoelectric areas.

Following Rabe's 2002 work, Hurley *et al.*[29] investigated the use of the AFAM technique on niobium thin films. To further develop the theory behind the technique they explored the effect of tip geometry, contact theory used and the reference sample on the final outcome of an AFAM experiment. The results of their experiments proved how sensitive the AFAM technique can be not only to the cantilever geometry but also to the reference material and model used. Results, seen in Table 1, show indentation moduli ranging from 86 - 127GPa for the same sample using different testing conditions. Hurley *et al.* was able to prove how important it was to choose the correct parameters and materials before beginning the experiment, in order to obtain a reasonable result. First, the selection of a suitable reference material proved to be vital[49]; a suitable reference material should have a similar Young's modulus to the material you are investigating as it will give a good estimation of how your sample will react under experimental conditions. It is hypothesized that the selection of non-suitable material as a reference could lead to a difference in contact between the surfaces, making a commonly used Hertzian model deviate even further from realistic values.

Cantilever	Reference	Model	Modulus (GPa)
Rectangular	Glass	Analytical	88±9
		FEM	89±11
	Si	Analytical	127±7
		FEM	126±8
	Average	Analytical	106±12
		FEM	106±14
Dagger	Glass	Analytical	86±2
		FEM	86±3
	Si	Analytical	127±5
		FEM	118±4
	Average	Analytical	105±5
		FEM	101±5

Table 1 AFAM values for the indentation modulus *M* of a Nb film. The indentation modulus was determined using verious types of cantilever, two reference materials, and two analysis model. The evaluation shows the dependence of the indentatiom modulus values of a number of outside influences

Similar to Hurley *et al.*[29], Kopycinska-Müller *et a*l.[30] and Passeri *et al*.[31] used the AFAM technique to investigate the indentation modulus of thin films. Building on Hurley's experiments Kopycinska-Müller *et al.* aimed to understand how the thickness of the films would influence the indentation modulus reported. The Passeri group explored the ability of the AFAM to differentiate between the various phases on the thin film's surface. Kopycinska-Müller *et al*., measured three nickel films approximately 50, 200, and 800 nm thick respectively; the resulting indentation moduli of 210±26, 220±19 and 223±28 GPa were reported. The calculated values were lower than expected and the results attributed to the reduction in the elastic modulus in nanocrystalline materials caused by closed porosity and/or impurities introduced during the deposition process of the thin films. However, the consideration of cantilever and tip properties were neglected in the indentation modulus calculation. Passeri *et al.* were successful in measuring the indentation modulus of tin-selenide ultrathin films, which was estimated to be between 35-55 GPa. The range in values was explained by the AFAM's nanoscale ability to detect different mechanical properties of the two crystalline phases (SnSe and $SnSe_2$) comprising

the film. The ability of the AFAM to detect the properties of the supporting substrate below the thin films is a point of contention between the two papers. Kopycinska-Müller *et al.* reported that the AFAM technique was not sensitive to the substrate, which represented an improvement over the nano-indentation method. However, Passeri *et al.* reported that the substrate was indeed influential in the final result. In Passeri *et al.*'s paper, the initial indentation modulus ranged from 54-68GPa but further calculations eliminating the influence of the substrate reduced the modulus to 35-55GPa (Figure 7). This difference is most likely caused by the thickness of the film. Passeri *et al.*'s SnSe films had a 22nm thickness, less the half the thickness of the thinnest film used in the Kopycinska-Müller *et al*. In 2010, *Mège et al.*[32] also showed how the subsurface features of a sample can influence the AFAM data collected. In their paper a porous silica thin film was imaged, and the stiffness variations characteristic of the underlying porosity were clearly seen in the AFAM images (Figure 6). An examination of the height of the AFM image showed that the sample was rather flat, RMS =3.4 nm, so the AFAM image was barely influenced by large changes in height. The image was then the result of a softer material at the heart of the "hollow spheres "and a stiffer material" towards the edge. The stiffer edges of the "hollow spheres" had Young modulus values close to the calculated values of dense silica when using static testing.

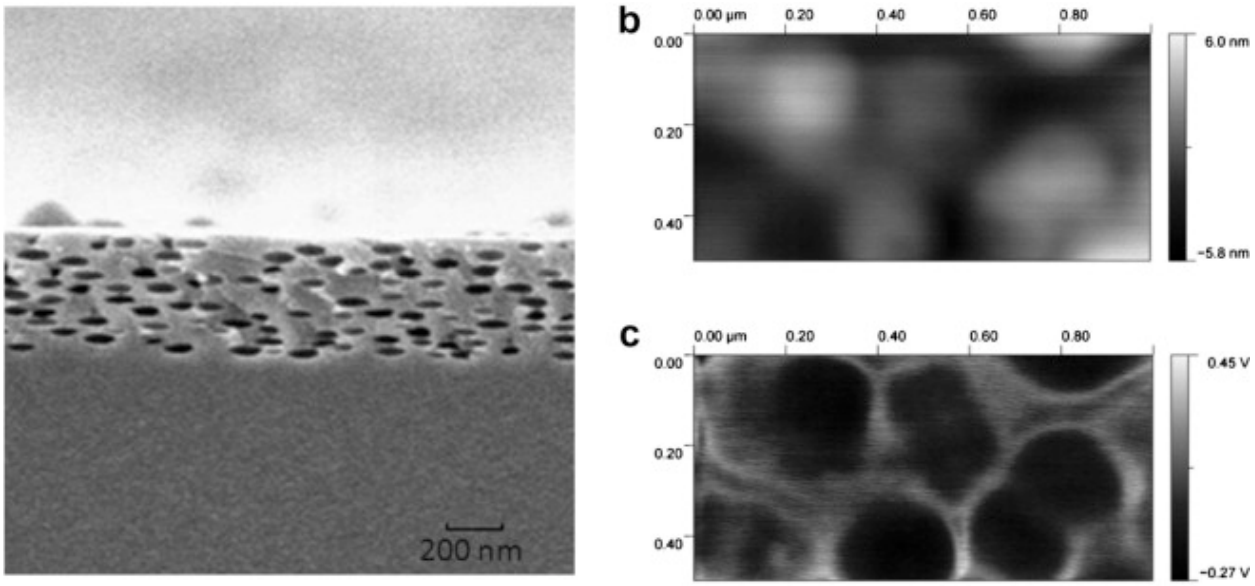

Figure 6 (a) SEM of macroporous silica of 70 nm (b) AFM topography (c) AFAM imaging at first flexural mode. In (c), it can be seen that the AFAM was able to detect the presence of hollow spheres seen below the surface in (a). The AFAM is able to detect these areas because the hollow spheres result in the surface directly above having a lower elastic modulus.

In order to check its reliability, the AFAM technique is frequently used in conjunction with the nanoidentation technique to investigate the Young's modulus of materials. Kassavetis *et al.*[33] investigated hydrogenated amorphous carbon thin films and found that the AFAM values were in all cases higher than the values determined though nanoindentation. The researchers explained that this discrepancy was probably due to the difference between the forces applied to the substrate in each method. Because there is no need for a tip to oscillate, the tips used during a nanoindentation test are traditionally much stiffer than the tips used during an AFAM scan. When using a stiffer tip, the tip is able to penetrate into the surface of the sample, causing an indentation. However during an AFAM scan there is little to no indentation into the surface, and the applied force is significantly smaller than that used during nanoindentation. Even for harder materials, the applied force during a mechanical testing can have an impact on the material's response and hence affect the reported results.

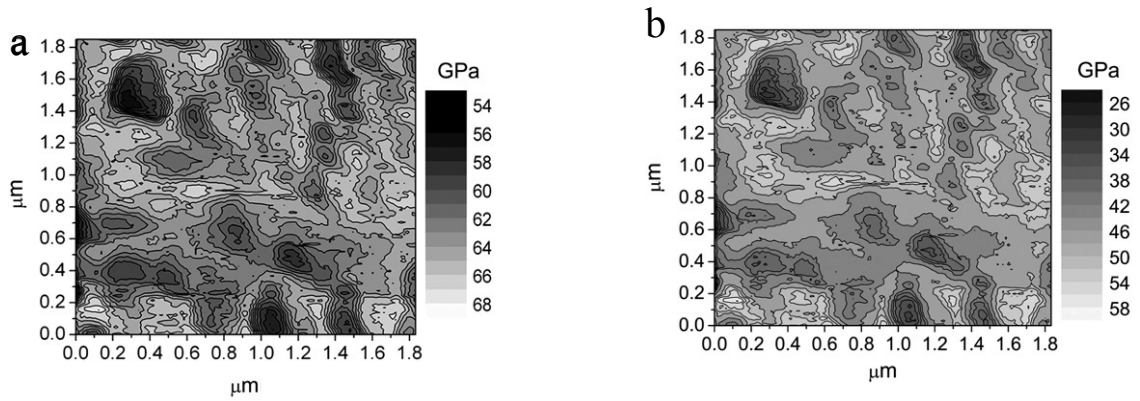

Figure 7 - Reconstructed pattern of the indentation modulus values before (a) and after (b) adjusting for the effect of the underlying substrate.

In 2006, Stan and Price[34] aimed to prove the benefits and drawbacks of the dual reference surface method suggested by their predecessors. In using dual reference surfaces, the assumption of constant tip elastic properties is ignored, which could, in turn, lead to a more accurate Young's or indentation modulus. When the elastic properties of gold were measured using CaF_2 and Si as references, the indentation modulus were only off by 3.6±0.8 GPa from its theoretical value, a vast improvement when compared to other methods. The measurements were achieved by eliminating the dependence of tip shape or location, which is vital in other calculations. Though it seems to be more precise than previous methods, it requires significantly more calculations.

2.3.3. Using AFAM to detect phase differences in materials

While AFAM has been extensively used to characterize the mechanical properties of materials, AFAM has also been used to detect the difference between phases[31]. Using piezoelectric materials that are known to have varying elastic properties depending on the orientation of the piezoelectric axis, Banerjee *et al.*[35] investigated the AFAM's ability to sense these small differences. Scanning both above and below the resonant frequency, the AFAM

delivered frequency maps that clearly distinguished between the two regions of a polycrystalline lead zirconate titanate (PZT) sample. The AFAM images were able to illustrate which parts of the sample where aligned in the longitudinal axis, signaling a softer material (Figure 8). A similar study done by Zeng *et al.*[36] used low-frequency AFAM on $Pb(Mg_{1/3}Nb_{2/3})O_3–PbTiO_3$ single crystals observing similar behavior within the piezoelectric material. Furthermore, Karagiannidis *et al.*[37] was able to

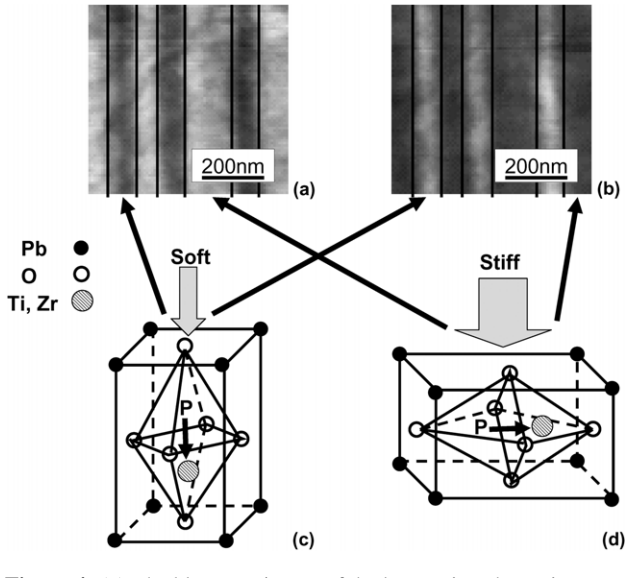

Figure 8 - Schematic representation of the PZT unit cell and orientation of the axis with respect to the probing tip, the soft and hard axes. (a) and (b) AFAM images carried out above and below the resonant curve, respectively. (a) showa stiff (bright) and soft (dark) stripe regions of the PZT unit cell while (*b*) shows stiff (dark) and soft (bright) stripe regions of the same area (c) and (d) The schematic representation of the PZT unit cell and orientation of the axis with respect to the probing tip, the soft and hard axes. The stiff and soft regions with respect to each orientation are shown by arrows. The AFAM is able to detect and deliver sharp images between the two different piezoelectric materials.

use the AFAM to discover a previously unknown nanolayer of amorphous poly(3-hexylthiophene) polymer surrounding fullerene derivatives. This nanolayer could have not been detected using microscale mechanical testing methods or optical microscopy.

Similar to the behavior of polymers, different crystalline orientation and experimental conditions can affect the elastic properties of titanium. Kumar *et al.*[38] used AFAM to study the differences between elastic properties of α and β phases in a Ti–6Al–4V alloy as it has been previously shown that the mechanical properties of these phases were highly dependent on thermal/thermo-mechanical treatments[39]. The closely packed hexagonal Alpha phase is more prevalent at lower temperature while the cubic structured metastatic Beta phase is seen more at higher temperatures[40]. The AFAM image, illustrated in Figure 9, show that the technique was not only able to distinguish between the two phases but also it was able to sense the different orientations of the different crystallographic orientations of the alpha phase. Using nickel as a reference sample, Kumar *et al.* found the indentation modulus to be 110 GPa for the beta phase and a range between 120 –130 GPa for the various alpha phases. All the values gathered were in good agreement with previous measurements on single-crystals[41].

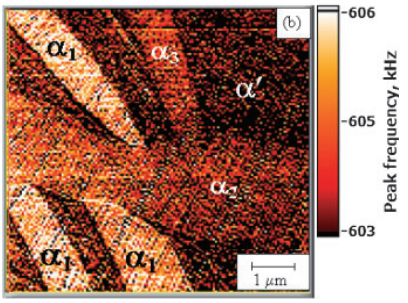

Figure 9 Distribution of the first contact-resonance frequency in Ti–6Al–4V. The three different variants of alpha phase are marked as α_1, α_2, and α_3. The AFAM technique was easily able to distinguish between the different orientations of the alpha phase different crystallographic orientations and show that each phase resulted in a different contact frequency which will result in different calculated elastic moduli.

Stehlik et al.[42] used AFAM to determine whether the two glass transition temperatures seen during modulated differential scanning calorimetry of $Ag_x(As_{0.33}Se_{0.67})_{100-x}$ chalcogenide glasses were influenced by differences in local elasticity and stiffness. As expected, AFAM

images showed that the pure chalcogenide glass was relatively homogenous, however as the percentage of Ag increased, grains showing darker and lighter areas emerged. Although AFAM was initially intended to prove their hypothesis that there had been phase separation in the glass, the results were inconclusive due to the multiple variations in the AFAM methodology including the surface's smoothness and how securely the sample was fixed onto the transducer. Regardless of the undesired outcome of the test, AFAM was able to show that there was an inhomogeneity in the local stiffness of the sample and that further testing needs to be done to determine if this inhomogeneity is indeed due to phase separation.

Zeng *et al.*[36] investigated piezoelectric behavior of $Pb(Mg_{1/3}Nb_{2/3})O_3–PbTiO_3$. AFAM scans of the specimens were found to be identical to the piezoresponse image indicating a relationship between mechanical and piezoelectrical behavior. The lighter areas in Figure 10 show a high contact stiffness and this increased stiffness corresponds to greater piezoelectricity. Zhao *et al.*[43] provided further proof of the relationship between piezoelectric response and contact stiffness, confirming Zeng *et al.*'s findings.

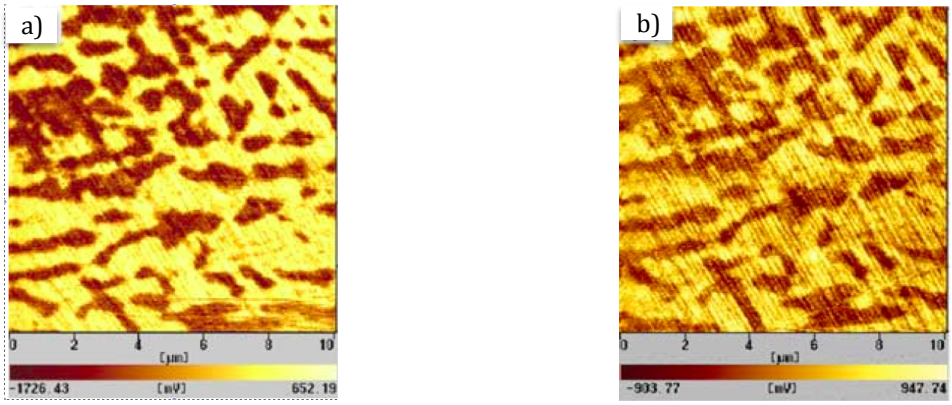

Figure 10 a) Acoustic image of $Pb(Mg_{1/3}Nb_{2/3})O_3–PbTiO_3$ single crystal b) piezoresponse $Pb(Mg_{1/3}Nb_{2/3})O_3–PbTiO_3$ single crystal

As the years progressed, researchers confirmed that the nanoscale properties of thin films were different from the bulk elastic properties. In 2010, Mangamma *et al.*[44] sought out to explore

how the nanoscale topography of silicon carbide (SiC) affected the strength of their material. Using AFAM, showing that the nanoscale topography consisted of clusters of grains of various sizes[45,46], and also that the boundaries at which these grains came together was ten times stiffer than the interior of the grains. They also noted that as thickness of the film approached and exceeded 150 nm, the stiffness and the modulus of the film increased, approaching the bulk value for SiC.

It is important that AFAM scans are done at a resonant frequency close to that of the contact resonance frequency. He *et al.*[47] showed how scanning outside the contact resonance frequency can affect the contrast on the images. He *et al.* performed scans at various contact frequencies and various applied loads and concluded that the contact resonant frequency for the first flexural mode was approximately 675 kHz. Three scans at 650 KHz, 700 KHz and 900 KHz were subsequently done. The first two scans, done above and below to the contact resonant frequency show a high degree of contrast while the image at 900 KHz showed a drastic decrease in the ability of AFAM to display the contrast seen in the previous two images. This behavior was due to the decrease in excitation amplitude of the cantilever.

2.3.3 Previous Applications of the AFAM Technique – Non-Metals

Prasad[48,49] in 2002 used AFAM on a softer material, clay, and noticed that it was increasingly difficult to obtain images using the traditional scanning technique, Therefore they switched to point by point measurements. An average Young's modulus of 6.2 ± 2.5 GPa was obtained, while the experiment values were highly reproducible, a large 40 percent error was a cause of worry. As with previous works[,26], this discrepancy was attributed to approximation of beam geometry and tip shape, Further investigation was done in 2007[49], and the indentation

modulus was found to be 9.9 GPa ± 3.3 GPa, which is in greater agreement with the theoretical value of 10–12 GPa[50]. However, the beam geometry was not measured and it was instead inferred.

As the AFAM technique began to mature, researchers began to explore other uses for the AFAM. Most of the polymers probed were thermoset epoxies sometimes filled with another material such as glass[51,52] or carbon nanotubes[53]. One of the first occurrences was the quantitative AFAM scan of a glass fiber embedded in a polymer matrix performed by Hurley *et al.* in 2005. The sample was scanned at 0.2 Hz for 22 min using a cantilever of unspecified contact stiffness. Following the scan, the AFAM was able to clearly detect the differences in stiffness between the two materials with the circular glass fiber appearing much lighter than the surrounding polymer. Upon calculating k^*/k_c, the reduced contact stiffness values for the polymer was determined to be approximately 50-100, while that of the glass fiber ranged between 100-250. Though the Young's modulus was not directly calculated, a higher contact stiffness value is a good indicator of a higher Young's modulus. Also notable in this paper was the ability of the AFAM to recognize not only the differences between the polymer and the glass fiber but also difference within a single glass fiber. Results from the AFAM scan indicated that the center of the fiber had a lower contact stiffness than the surrounding peripheral areas of the fiber. In 2011, Karagiannidis *et al.*[54] also used AFAM to detect differences within a single material. For this experiment, the researchers were investigating the nano-scale mechanical properties of a poly(3-hexylthiophene) (P3HT) and fullerene derivatives (PCBM) composite blend. The results of the scan noticed the higher contact stiffness materials as the lighter shades, with the weaker materials in gradually darker shades. Analysis of the scans showed that P3HT polymer aggregates closer to the interface of the PCBM, were darker than the images of the

surrounding PCBM. It was theorized these P3HT aggregates were composed of amorphous P3HT. Though the research in both of the previously mentioned papers used AFAM technique to detect the differences in the mechanical properties of their component composites, neither presented quantitative Young modulus data.

Preghenella *et al*.[55] were the first to report quantitative Young's modulus data following their analysis of epoxy-silica nanocomposites. Silica particles were dispersed in a DGEBA-based low molecular weight epoxy resin at varying weight percentages ranging from 0 to 16.7 percent. The samples were scanned using a non-contact tip with contact stiffness of 5.5N/m. The Young's modulus values reported ranged from 2260±71 MPa for the silica-free sample to 2800±240 MPa for the sample loaded with 16.7 percent silica. In 2007, Passeri *et al*. also used the AFAM technique to analyze nanocomposites of purified SWCNTs (1 wt%) into bisphenol-A/epichlorohydrin-based epoxy resin. Unlike Preghenella *et al.* the values obtained were higher than expected, ranging between 6-18 GPa, using the dual reference method with Al and PA-GPR as reference materials. The researchers attributed these values to the possible presence of nanotube agglomerations that could be detected by the AFAM probe. Because of this, the authors of the paper decided to calculate Young's modulus data as a qualitative representation of the varying mechanical properties. This variation from the expected values can also be attributed to the use of reference materials to obtain the radius of the tip being used in the Hertzian equation. Using the single reference sample approach as done by previous researchers, with Al used as the reference, values ranging from 5-60 GPa were recorded. In 2009, epoxy degradation became a topic of interest for Zhao *et al.*[56] while working with carbon fiber epoxy composites. Using point-by-point testing similar to those performed by Prasad *et al.*[48], Zhao *et al.* observed that

there was a decrease in the elastic modulus as the boiling degradation time of the epoxy increased.

Liu *et al.*[57] also used the AFAM technique to correlate mechanical properties with material properties in their study of electrospun semicrystalline polymer fibers. Using the AFAM technique to measure the stiffness of the fibers, they were able to see a clear correlation between fiber diameter and stiffness. The work by Liu *et al.* is particularly interesting because it is one of the few published worked to focus primarily on fibers, which is the main focus of the study for this research work. By correlating the AFAM measurements with shear modulation force microscopy (SMFM) and finding good agreement between the two measured values, they are also able to prove that the AFAM technique can be a useful tool for measuring the modulus values of small fibers.

In addition to polymers, the AFAM technique has also been used on other non-metals such as cement. Seeking to overcome the limited spatial resolution of nanoindentation, *Kim et al.*[24] used the technique to measure the elastic properties of cement pastes and determined an AFAM modulus of 14.7±20.5 GPa, while nanoindentation resulted in values of 20.5±7.58 GPa. The discrepancy between the two reported values was most likely due to the difference in contact area between the sample and the tips. The AFM tip had a radius in the order of 30 nm while the nanoindentation tip was around 1μm. The smaller spatial resolution of AFAM tips allows it to be much more sensitive to the non-homogeneity of the sample surface hence resulting in the wider range of values. The researchers were very careful to measure and confirm cantilever dimensions, resulting in a high level of confidence in their findings.

2.3.4 Influence of Tip Characteristics on AFAM results

In order to calculate the Young's modulus, determining the radius of curvature of the tip is an important factor. As the tip scans over the sample, the radius of the tip will increase due to tip wear[58],[59] and this increase in tip wear can have a significant impact on the calculated Young modulus value. In order to calculate the radius of the cantilever tip, two methods are usually employed: 1) using a reference material and one of the contact mechanics theories to deduce the radius or 2) looking at the tip using an SEM and directly measuring the radius. In 2005, Kopycinska-Müller *et al.*[58] found that these two methods are not usually in agreement. The radius obtained from the SEM was 25 nm while the radius using the reference method, indicated a tip radius of 13±3 nm. This discrepancy arises from the assumption that the tip radius remains constant during the measurements. In reality, the tip radius is continuously changing; this change depends on the applied static load and the elastic properties of the sample. The researchers were also able to show that the Hertzian assumption that the radius is independent on the applied load was invalid. In order to minimize the effect of tip wear, the use of coated tips has also been employed. Amelio *et al.*[59] found that probing a high stiffness sample such as diamond layer coating caused high wear on non-coated silicon tips. It was found that the utilization of diamond coated tips caused a drastic reduction in tip wear and hence a more stable signal during the AFAM scanning process. Both Kopycinska-Müller *et al.* and Amelio *et al* found that while most tip radii would increase after an AFAM scan, they still maintained their proposed hemispherical shape. This capacity is critical to the application of most contact theories. Marinello *et al*.[11] was able to go even further and showed that the tip radius can change at a rate of 1-2 nm/min using standard silicon tips. This behavior can result in changes in the tip diameter of 40-50 nm during a standard scan. Reinforcing Amelio *et al.*'s finding, the use of coated tips was found to reduce the

rate of wear by a factor of 2–5. Unfortunately coated tips tend to have larger diameters and can result in more erratic results[60].

Even with reduced tip wear, another important component in ensuring correct AFAM modulus results is using the right model to simulate the tip-sample interactions between the tip and the sample. The most commonly used interaction model is the Hertzian model, modeling the cantilever tip as a sphere and the substrate as a half space. However modeling the tip as a sphere is not the only option, as proven by Zhao *et al.*[61] during their study of epoxy composites. As seen by previous researchers, after an AFAM scan the cantilever is usually no longer a sphere, but more similar to a flat punch with rounded edges (called round punch by Zhao *et al.)*. The researchers explored the change from the spherical tip assumption and found that by changing the model used to relate the contact stiffness to the Young's modulus, there was a change in the calculated elastic modulus. Using both indium and Epon 862, there was a decrease in the calculated Young's modulus when changing the interaction model from the Hertzian model to a new power-law shaped body of revolution model.

2.4 Bicomponent Fibers

The fibers used for this research are bi-component nylon-polyethylene terephthalate (PET) island-in-the-sea fibers produced by Hills, Inc. Bicomponent fibers were first introduced commercially in Japan in late 1960's for use as synthetic suede fabrics[62]. Bicomponent fibers, as the name suggests, are made up of two different polymers that are spun together through one spinneret[63]. Bicomponent fibers can be produced in different configurations including side-by-side islands-in-the-sea fibers, fibers, or shealth-core fibers as shown in Figure 11.

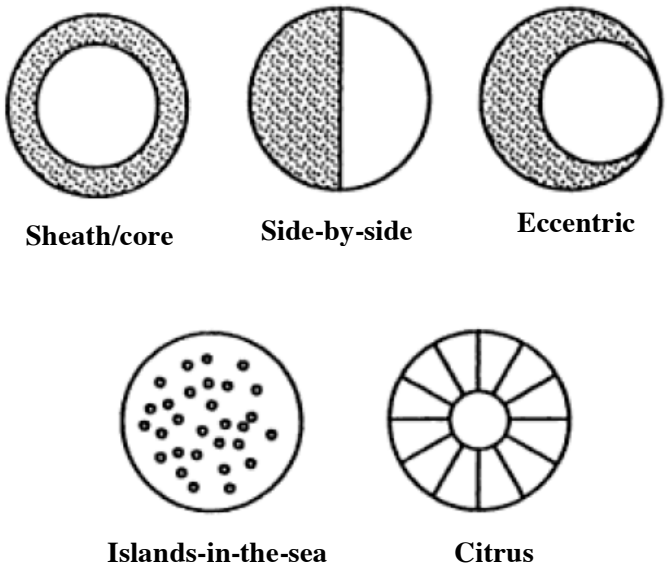

Figure 11 Configurations of various bicomponent fibers. The light and the dark areas represent two different type of polymers[63]

Islands-in-the-sea bicomponent fibers are fibers in which many small domains of one polymer are dispersed in the matrix of another polymer[64]. The sea is usually made up of number of dissolvable polymers including polystyrene, co-polyesters (COPET), polyvinyl alcohol (PVA)[65]. There are several methods used to produce island-in-the-sea fibers which can be found in various US patents[66,67,68]. Moriki et al.'s[67] approach involved creating multiple shealth/core streams and combining them into one conjugate island-in-the-sea fiber in the spinneret. Using this method, Moriki et al.[67] was able to produced island-in-the-sea fibers with up to 126 islands. Kiriyama et al. proposed mixing different polymer streams in a mixer, which divides and re-divides a multicomponent stream, forming a stream with hundreds, or thousands, of cores within a matrix. However, this method leads to non-uniform islands and the formation of non-continuous island filaments. The most widely successful method, patented by Hill Inc. involves two separate polymer streams which pass through filters, metering plates, distribution plates to form a

conjugate stream. Fiber diameter, cross sectional area, and the number of islands depend on the diameter and the shape of the spinneret orifice and the polymer distribution in the distribution plates. Hills, Inc. has been able to produce fibers with up to 3000 island fibers within a single microfiber[62].

3. Materials and Methods

3.1 Fiber Preparation

Nylon/PET island-in-the sea fibers obtained 3G, LLC(Cary, NC) and provided by from Hills Inc. (Melbourne, Fl) were first cut into approximately 2 cm long pieces. A bundle of fibers consists of roughly 70 fibers; therefore, in order to keep the bundle together one end of the fiber bundle (~0.5 cm) was affixed to a tape. Once the bundle was secured the excess tape was removed using either a razor or a pair of scissors. The end without tape was placed in a BEEM® Capsule Bottle Neck Tip (EMS; Cat: 69912-05) with the taped end sticking out the capsule.

3.2 Epoxy Preparation

2.9 grams of Embed resin, 1.6 grams of DDSA, 1.43 grams of NMA and 0.17 grams of BDMA were added to a beaker and carefully stirred. Because BDMA is a crosslinking agent, it was the last ingredient, carefully added during the stirring step. The solution was stirred slowly in order to avoid introducing bubbles, as bubbles could lead to cracking in the sample in subsequent processing steps. The 1:0.55:0.49:0.06 ratio of the aforementioned chemicals produced a medium strength resin.

3.3 Epoxy-Fiber Preparation

After the epoxy solution was stirred, it exhibited a bright uniform orange color. If there are any streaks of yellow within the solution, this is an indication that the BDMA is not well distributed in the solution. Once the solution was uniform in color, a small amount of solution was poured into a BEEM® capsule, filling it approximately half way. Using a 9” disposable glass pipette, excess air was carefully removed from the bottom of the capsule, to avoid removal of the

embedded fiber. Once all the air bubbles were removed, the remaining space in each capsule was filled with the resin solution. The sample was placed in an 60°C oven for 24 hours to cure, then removed from the oven and allowed to cool at ambient temperature.

3.4 Microtoming

For AFAM scans, it is important to have a flat sample surface, as sample topography can influence your results. In order to expose the cross section of the island-in-the-sea fibers and flatten the surface the samples were microtomed. Microtoming involves gradually removing small sections from the small surface until the desired surface flatness is achieved. The fiber/epoxy matrix was placed into the specimen holder and the clamping screw tightened to ensure that the block was firmly fastened into the microtome holder. Then, a carbon steel razor blade was used to cut an initial 1mm chunk from the top in order to initially expose the cross section. If the fiber cross sections were not seen after this step, smaller (~0.25-0.5 mm) sections were cut from the top until the cross section was seen under the microscope. Once the cross section was exposed, a single fiber was chosen and the surrounding epoxy/fiber matrix removed. To further flatten the sample surface, a glass knife was used to remove 1μm sections from the sample surface. Following the glass knife, a diamond knife (Diatome) was used to remove 30-50 nm sections for approximately 5 minutes with the microtome operating at 0.6 mm/s. The objective was to produce a microtomed sample that was flat and with a reflective quality when exposed to light. A reflective sample surface is a good indication that the sample surface is flat, at least at the microscale. After the sample was microtomed, it was examined under a optical microscope to check for any surface imperfections, such as scratches caused by the microtoming.

Any imperfections that can be seen under the microscope indicates the surface at the nanoscale will also have defects.

3.5 Sample Imaging

3.5.1 AFM

Once the sample was prepared (microtomed), the next step was to analyze it using a NTREGA Prima (NT-MDT) AFM with a liquid SMENA head scanner. In order to begin the AFAM scans, it is important to first conduct AFM scans to determine the exact location of the fibers within the fiber/epoxy matrix. First, the sample was affixed to the AFAM transducer stage using a small amount of Instant Krazy Glue®. The stage was then placed in the instrument and allowed to equilibrate for about an hour. ensuring that any charge buildup from the microtoming process was removed. Next a CSG10/Au AFM cantilever, spring constant of approximately 0.40 N/m (spring constant calculation in section 3.2.1), was placed in the cantilever holder. After aligning the laser (DFL and LF both approximately zero) and maximizing signal strength (laser signal >25), the fiber sample was approached with feedback loop on. After the tip made contact with the sample, the feedback gain was slowly reduced until the DFL signal was stable (± 0.2 of the set point value). Next, a contact 30 x 30 μm AFM scan was performed at 1.0 Hz to locate the fiber within the matrix. For all AFM scans, height, lateral force and phase images of the fiber sample were typically collected. These images were collected in order to locate the fiber and also to check for surface imperfections that might affect the AFAM scans. Once the fiber was located, two additional AFM contact scans were performed. For the first one, the scan area was reduced to a 12 x 12 μm. For the second, the scan area was further reduced to a 1.5 x 1.5 μm area. Once the appropriate scan area was chosen for each scan, the set point was adjusted

between 2 and 5 in 0.5 step intervals, until the lateral force image with the best contrast and detail was acquired.

3.5.2 AFAM

After the AFM scans were complete and a fiber within the matrix, free of scatches was found, the sample was analyzed using AFAM. The preliminary steps first include determining the resonant frequency needed for the AFM scans. To begin this, a frequency sweep was first done between 0 – 500 Khz with the amplitude parameter set to 1V and the lock-in amplifier set to 10, in order to locate the resonance frequencies. For all scans the first resonance frequency is chosen by narrowing the frequency sweep range. In the next step, the amplitude and lock-in gain amplifiers were adjusted until the Mag signal was between 8-10nA and the resonance peak was symmetrical.

a) b)

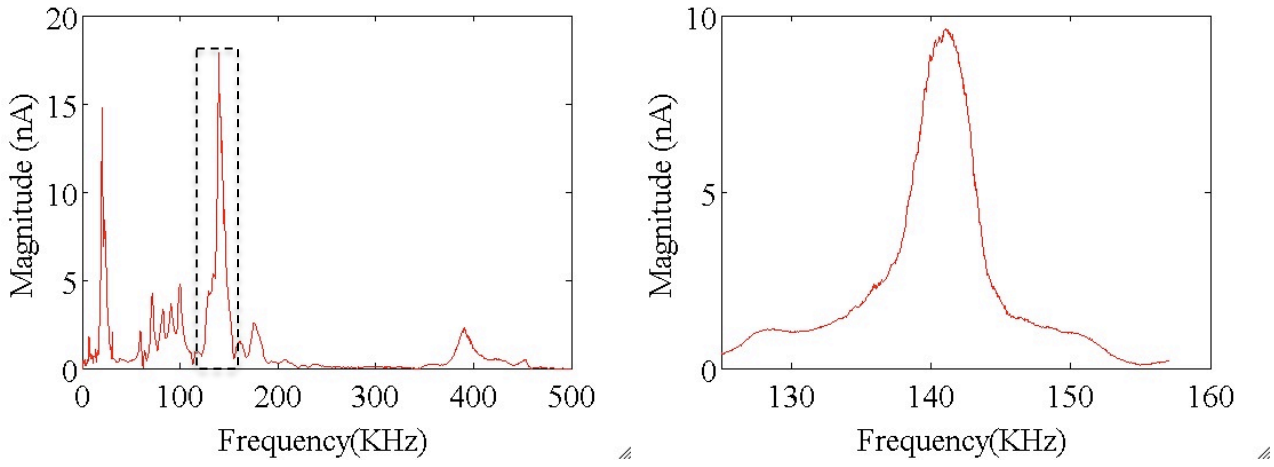

Figure 12 a) Frequency scan done before the an AFAM scan. A scan is done from 0 – 500 Khz to locate the resonance frequency. Once the appropriate frequency is selected, the scan range is narrowed and the magnitude signal adjusted to 8-10 nA (b)

For all scans the center of the resonance peak in selected for the resonance operation peak. The set-point was then re-adjusted ±3 points of the AFM set point, in 0.5 increments, until the set point that corresponded with the greatest shift in the position of the resonance peak was found. To begin the AFAM scan, the frequency scan speed was set to 0.45 Hz.

3.6 Cantilever Calibration

3.6.1 Spring Constant

In order to complete AFAM calculations, characteristics of the cantilever must be known, including the length, width and thickness. The length, width, and thickness are used to calculate the elastic constant of the cantilever. The elastic constant, k_c, for all cantilevers was calculated using Equation (11). All dimensions were measured using a Leica 440 SEM (Leica Microsystems, Wetzlar, Germany) which is located in the Cornell Center for Materials Research (CCMR). The length, width and thickness of the cantilever was determined, along with the radius using a point to point measurement program built into the SEM program. A sample calculation of k_c is seen below,

$$k_c = \frac{EWT^3}{4{L_1}^3} = \frac{(169x10^9\ \frac{N}{m})(3.3\ x10^{-5}\ m)(1.67x10^{-6}\ m)^3}{4(2.25x10^{-4}\ m)^3} = 0.59 \pm 0.12\ \frac{N}{m}$$

Cantilever	Length	Width	Thickness	Constant
1	225 μm ± 5 μm	33 ± 0.8 μm	1.67 ± 0.08 μm	0.59 ± 0.12 N/m
2	227 μm ± 6 μm	33 ± 0.8 μm	1.70 ± 0.08 μm	0.59 ± 0.12 N/m
3	225 μm ± 6 μm	33 ± 0.8 μm	1.49 ± 0.07 μm	0.40 ± 0.08 N/m
4	226 μm ± 5 μm	32 ± 0.7 μm	1.46 ± 0.07 μm	0.36 ± 0.07 N/m

Table 2 A sample of some of the cantilevers used in the AFAM measurements. The length, width and thickness are measured using an SEM

3.6.2 Force Distance Spectroscopy

After each AFAM scan, the force applied during the scans was measured by doing a force spectroscopy scan on a round piece of sapphire. With DFL selected as the signal output the left height was selected to be between 400-600 nm with 5 points within a 2μm area chosen to be tested. The force applied during an AFAM scan is a linear function of the probe displacement relative to the sample surface along the z-xis. By Hooke's Law, $F = k_c * \Delta\ height$, the force can be measured. Selecting the area between the point of retraction and the set point value, Δ height is obtained. Using the cantilever stiffness value calculated in Section 3.6.1, the force constant was obtained.

3.7 Young's Modulus Calculation

The contact resonance data collected from the AFAM software, as well as the recorded cantilever dimensions and force constant data were imported into a Matlab program (Appendix A) written using the equations described in Section 2.3.1.

4. Results and Discussion

4.1 Effect of Cantilever Change on Young's Modulus Results

The first set of experiments conducted was designed to test the effect of tip change by scanning the center most fiber as indicated in Figure 13. For all scans, a sample of topographical, lateral force and frequency images were recorded. An image of a sample scan of the center fiber scan is seen below in Figure 13. Also a MATLAB generated output of the calculated Young's modulus is shown in Figure 14

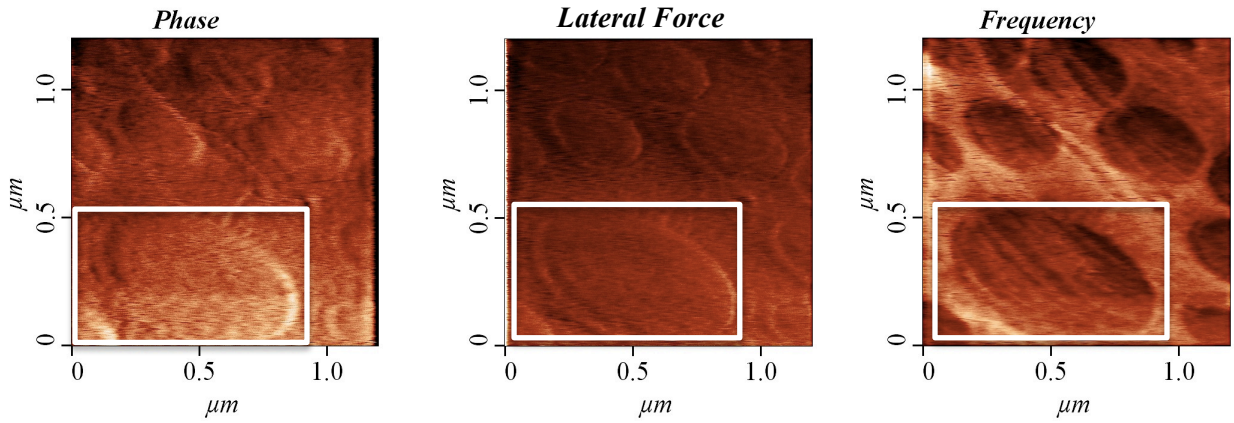

Figure 13 Phase, LF and Frequency images of the center most island (highlighted by the white box) of a NP3 fiber. All images are obtained during the same scan and provide different information about the sample surface.

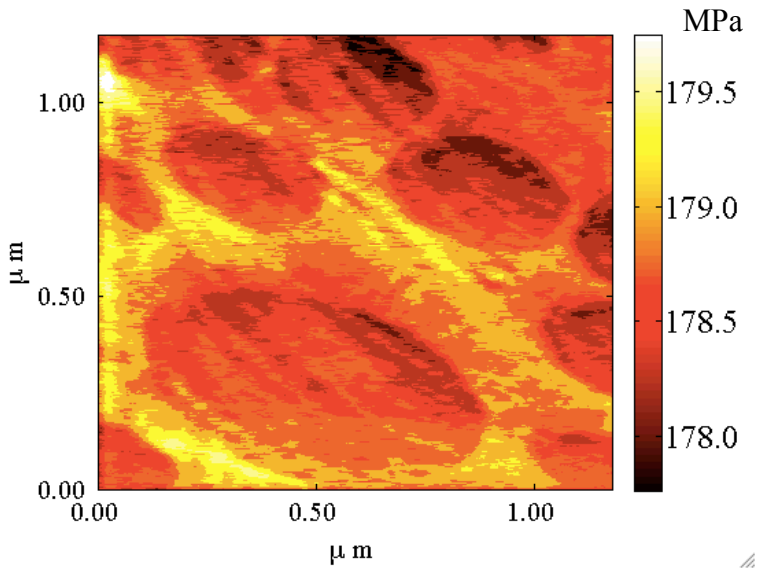

Figure 14 Young's modulus image using Matlab code in Appendix A of the center most island seen in Figure 13.

All scans were run under the same conditions: Applied force: 1.4 nN and ultrasonic transducer frequency 143 Khz, with each area being scanned three times. Each of the three consecutive scans were conducted on the same sample area under the same conditions, with one exception, a different cantilever was used for each scan. Each of the three scanned images demonstrated different resulting values for the Young's Modulus. The calculated Young's modulus values were 178.5 ± 21.1 MPa, 146.4± 16.9 MPa, 118.0 ± 14.0 MPa, as depicted in Figure 15. Though statistically there is slight overlap between the Young's modulus values, the results show there is significant variance with the values recorded using different tips for the same area.

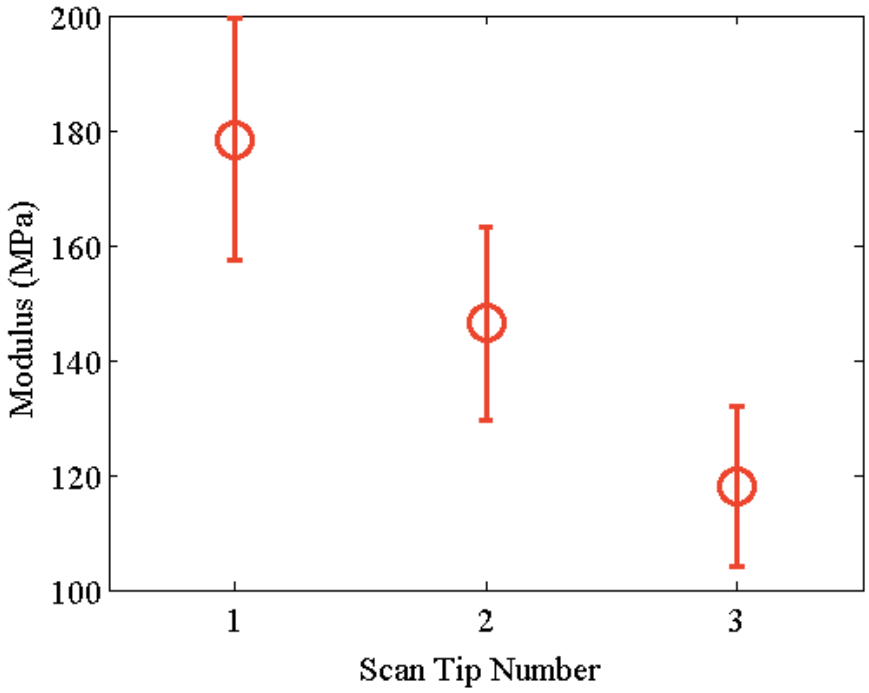

Figure 15 Comparison of the Young's Modulus on the center most domain of a NP3 fiber with a different cantilever used in each scan. The average calculated Young's Modulus values are 178.5±21.1 MPa, 146.4±16.9 MPa, 118.0±14.0 MPa.

From this series of scans, Figure 15, changing the tip appears to have a deeper impact on the reported Young's modulus values than previously hypothesized. This behavior may be attributed to various factors, such differences in tip mounting procedures. Tips can vary widely even within the same batch of cantilevers, even though the manufactur claims value on the packaging claims that the tip radius is 10±5 nm. Kopycinska-Muller *et. al*[69] showed that tips from a manufacturer packaged together can vary widely. Kopycinska-Muller *et al*. took SEM images of three new tips with reported tip radius values of 15±5nm from the manufacturer. Cantilever 1 and 2 both fit within the manufacturers reported radius with radius values of 10 and 20 nm. However the third cantilever imaged revealed a tip that was already blunt with surface contaminations that were not seen in the two other tips. Calculated Young's Modulus values obtained via AFAM were estimated using contact-mechanics models that assume simple

geometries of the cantilever tip, such as a sphere or flat punch. If the tip being used for the scan varies outside the spherical assumptions made in the calculations, all maybe invalid. Thus, by changing the cantilever tip for each scan, we may be introducing an additional dependent variable, tip geometry, into the calculations. The introduction of an additional variable could call into question the reliability of results.

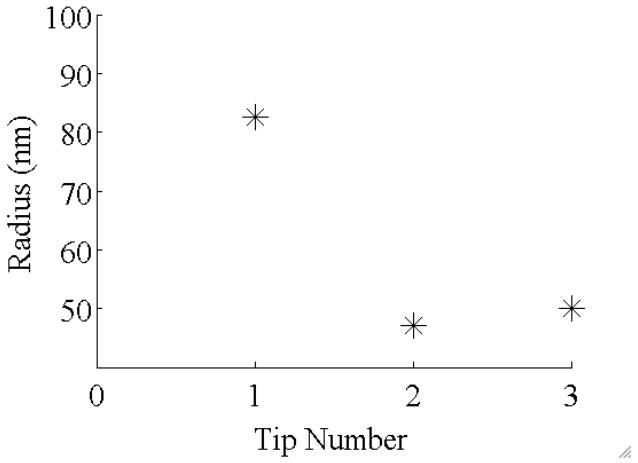

Figure 16 Tip radii of the three cantilevers used to produce the data in Figure 15.

We imaged the radius of all tips were measured at the end of each scan (Figure 16). However tips were not imaged beforehand, so we cannot be certain about the condition of the tips at the beginning of each scan.

When a randomly selected a cantilever was selected for further analysis using SEM, it indicated that the tip was blunt and contaminated as shown in Figure 17. This observation of the contaminated cantilever tip not only supports the observations made by Kopycinska-Muller *et al*., but it also further supports the conclusion that the geometry of the tip in the beginning of the scan can have a significant impact on Young Modulus results.

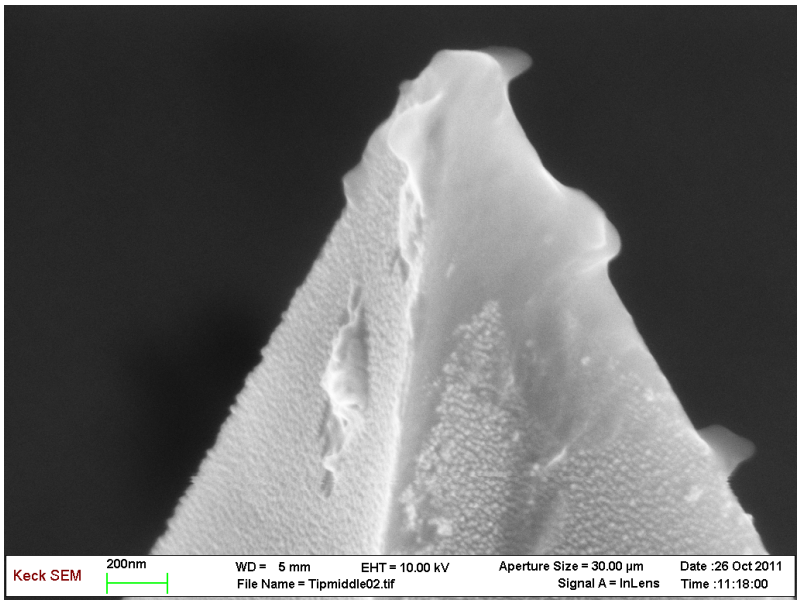

Figure 17 SEM image of a new CSG 10 Au-coated cantilever. Though new tips are supposed to have a semi-hemispherical shape with a radius <10nm, this tip is flat punch with radius of approximately 100nm.

Scans done on another NP3 fiber (Figure 18) show similar results to those seen in Figure 15. There is some overlap between the first two scans but then a significant drop is seen in the third recorded value.

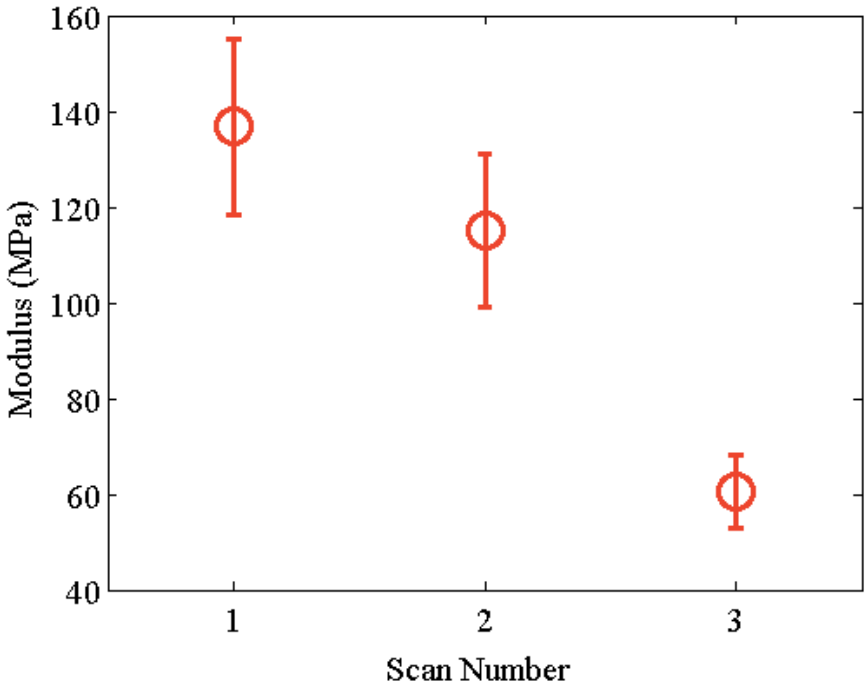

Figure 18 Comparison of the Young's Modulus done on acenter-most domain of another NP3 fiber with a different cantilever used in each scan. The calculated Young's Modulus values are 137.7±18.2 MPa, 115.1±16.0 MPa, 60.5±7.8 MPa respectively.

Following the first set of experiments done with separate cantilevers, a similar experiment was conducted but this time, the dependent variable of tip change was removed. Kopycinska-Muller *et al*. showed that using the same cantilever for multiple scans produce Young's modulus results that can have as much as a 20% difference from the first scan to the last scan. The following experiments using the same cantilever were done to validate that results. Results are shown in Figure 19 indicating that the average results for the Young's modulus varied approximately 5 percent. The variation between measurements using the same tip was also smaller than that of measurements in Figure 15 and Figure 18. These results suggest that using the same cantilever to for all scans on one fiber is the best method to produce accurate reproducible results.

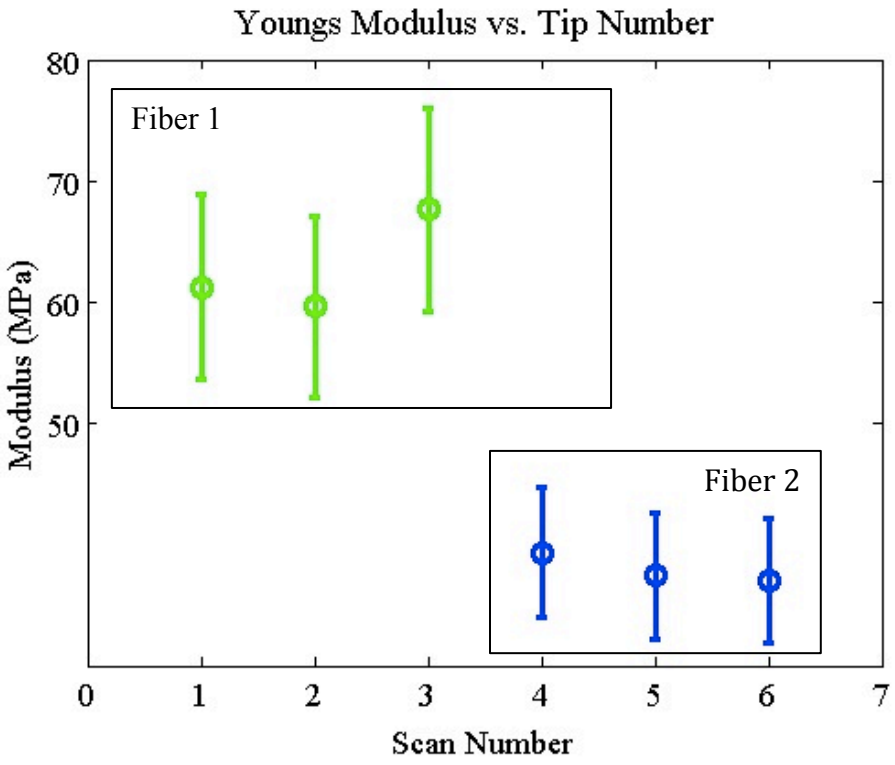

Figure 19 Calculated values of two separate NP3 center fibers scans. For both experiments the tip was not changed between runs. Comparing the values between runs indicates using the same tip for each run yields more reproducible results.

Comparing the results seen in Figures 15 and 18 to Figure 19 shows that in our experiments: 1) variations between cantilevers has a greater impact on the Young's modulus values than tip wear, and 2) tip wear does not appear to be a significant issue for soft materials such as polymers during an AFAM scan. At the beginning of this project, it was hypothesized that changing cantilevers would produce more reproducible results as it would eliminate the issue of tip wear which is a concern raised by many previous reports [11,59,60]. Our results suggest the opposite.

Though the exact reason for tip wear is not known, tip wear has been attributed to adhesion, plastic deformation, and abrasive wear during contact AFM scans[70,71.] Wear due to adhesion occurs when the two materials in contact move relative to each other, causing material

from one surface to be transferred to the surface of another material. Usually when adhesion forces are significant, transferred material can be seen on the tip which was not seen in any of the SEM images of the tips used in these experiments. However after reviewing SEM images of cantilevers, there was no evidence of significant material transfer, therefore adhesion is not significant in our AFAM measurements. Another possible type of wear is abrasion wear, in which a hard proturbance on a surface produces a groove, scratch or indention on the opposite surface. In previous experiments done where a smaller area of the fiber was scanned, immediately followed by the scan of the whole fiber, the area of the previous smaller scan can be clearly seen (Figure 20). Leading to the conclusion that the wear on the AFM tips is most likely abrasive wear. With abrasive wear, more wear is seen in the sample and the tip is not greatly affected. Abrasive wear results in the tip maintaining its shape for much longer and would help to explain the results seen in Figure 19.

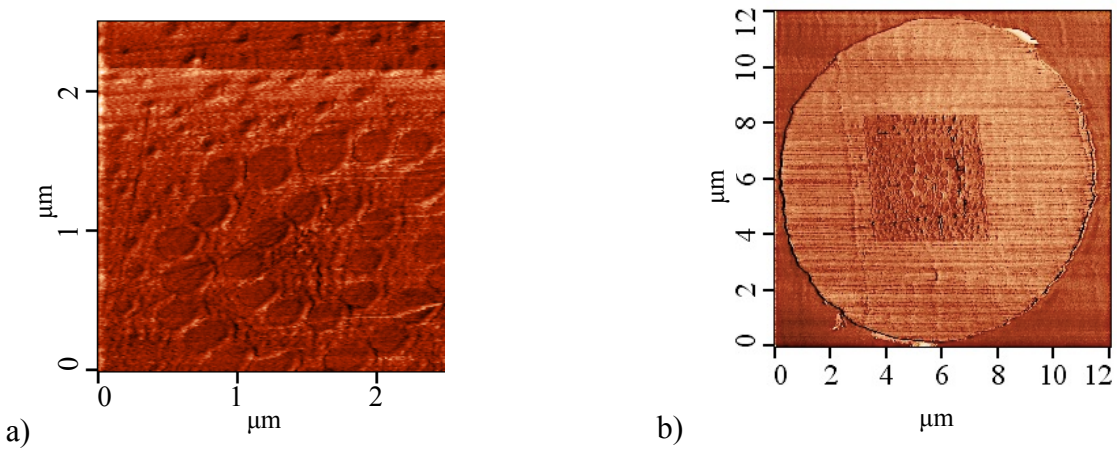

Figure 20 a) A smaller Frequency scan done before b) lateral force scan of the whole fiber. The area of the previous scan done can clearly be soon in the larger scan.

4.2 Elastic Modulus as a function of Radial Position

It is hypothesized that the Young's modulus of the island domains changes with radial position due to the way they are processed. In the specimens studied in this project, the larger domains (≈600nm) are located towards the center with the smaller fibers (≈100nm) towards the periphery.

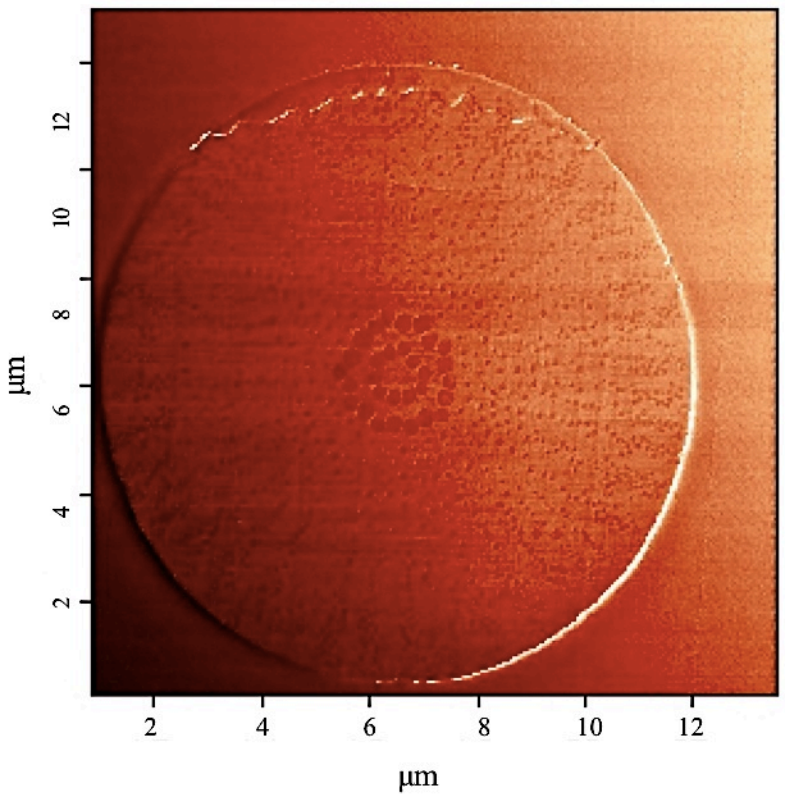

Figure 21 Phase Image of a bi-component PET/nylon fiber. The center most islands are approximately 600 nm, while the smaller peripheral fibers are approximately 100 nm.

Based on the size distribution of the fibers, it is expected that the Young's modulus will decrease with increasing radial direction. In order to test validate this theory, 1.5 µm x 1.5 µm sections were scanned from the center of the fibers to the outer domains. The results of a radial scan in the west direction are seen in Figure 22. Contrary to the initial hypothesis, there was no noticeable change in the Young's modulus as the radial direction change.

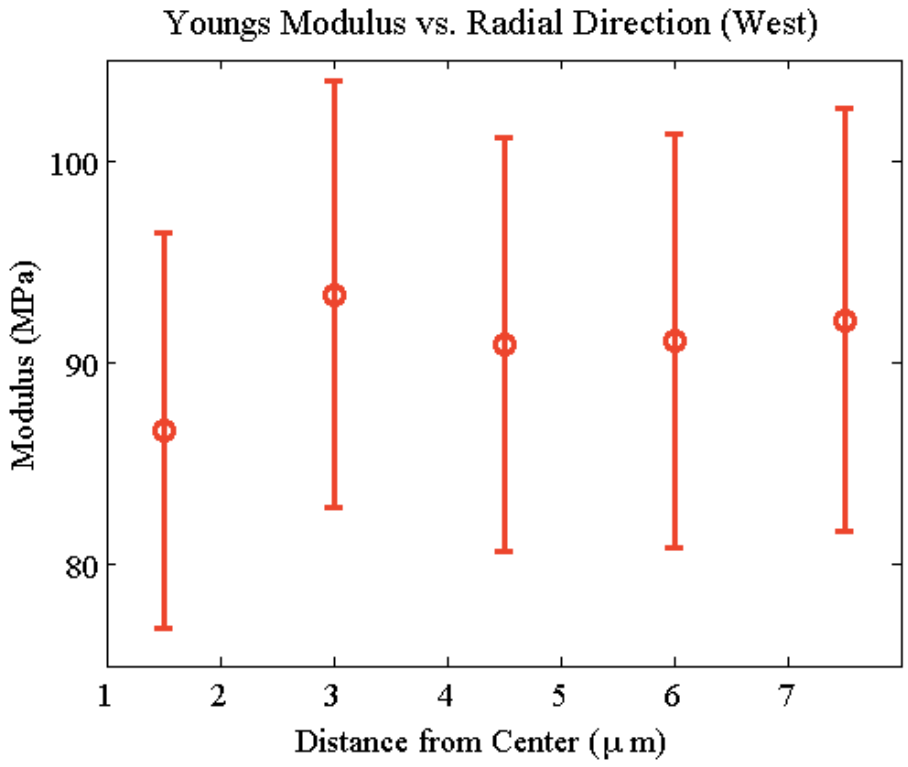

Figure 22 Results of AFAM Young's modulus measurements of a NP3 fiber in the west radial direction. The Young's modulus results vary from 86.7 ± 9.8 MPa to 92.2 ± 10.43 MPa. Within the margin of error for these measurements the Young's modulus values are considered to be similar. Leading to the conclusion that there is no change in the Young's modulus over the west cross section

Though there are nylon domains of different sizes within the bicomponent fiber, the size of the domains seem to have no influence on the Young's modulus values. The center most fibers tend to be larger in size than the peripheral fiber, which can clearly been seen in Figure 23. Starting from Figure 22a and continuing to Figure 22e, each scan gets progressively closer to the edge of the fiber. Regardless of the non-uniformity of the nylon domains in the bicomponent fiber, the size appears to have no influence on the Young's modulus. Unlike previous works where researchers have been able to link differences in features within an AFAM image to differences in modulus, the results seen here show no such connection[37],[38].

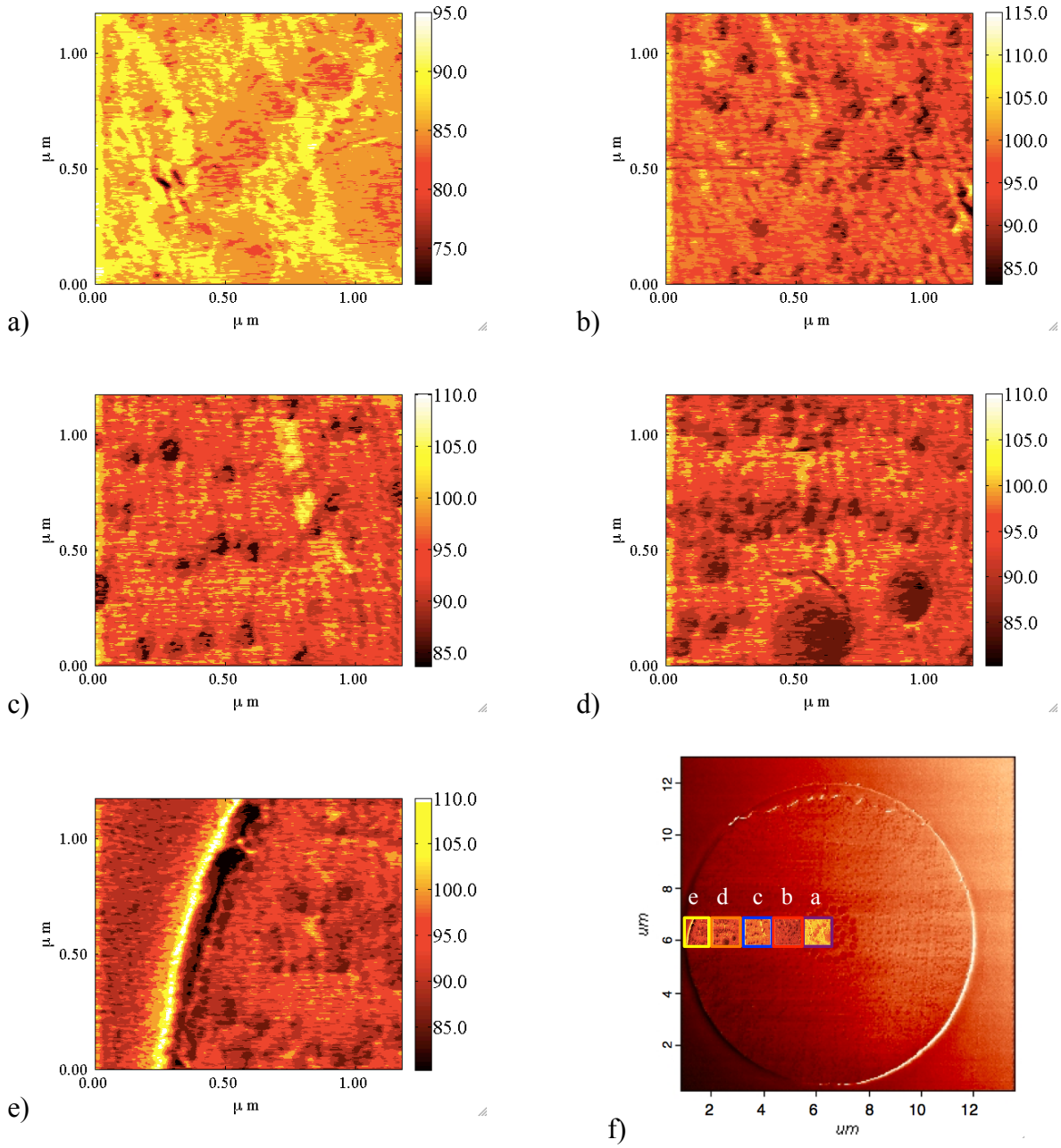

Figure 23 Young's modulus mapping of the NP3 fiber. The center most scan is seen in Figure 23a, while the peripheral scan is seen in Figure 23e. The larger islands towards the center can clearly be seen while the smaller islands are dispersed towards the edge of the fiber. Though the fiber cross-section of the fiber itself is non-uniform, the Young's modulus values that correspond to the nylon domains appear to be very uniform. Figure 23f shows the whole fiber and the 1.5x1.5 µm scans of Figures 23a-e.

In order to verify whether this uniformity in fiber Young's modulus distribution was the same for other radial directions, similar scans were done im the north and south directions for the same NP3 fibers and the results are seen in Figure 24 and 25.

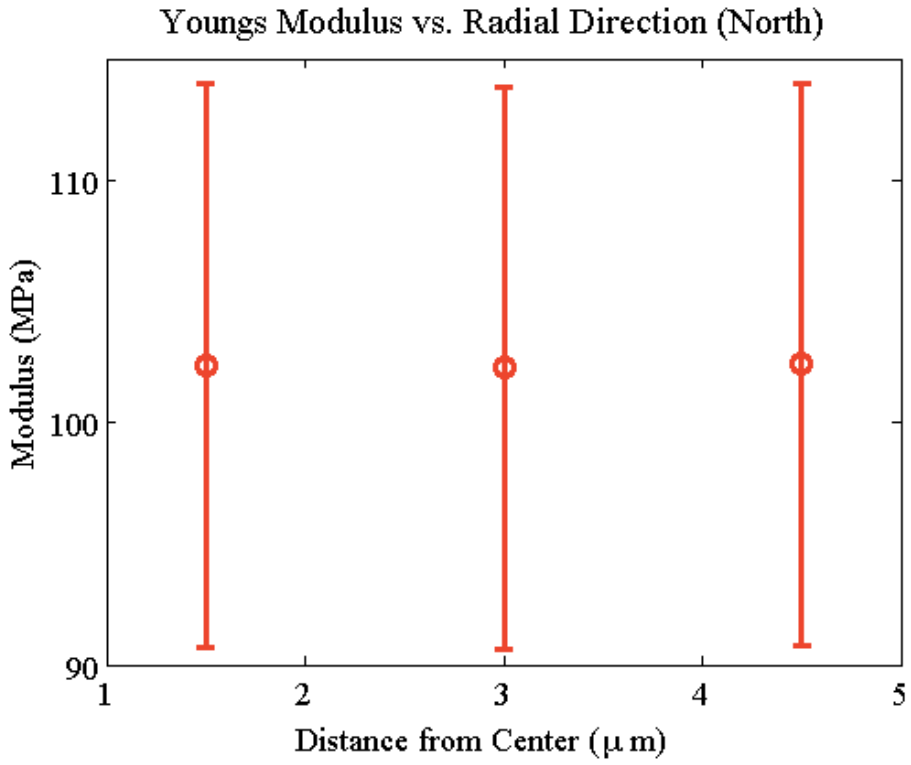

Figure 24 Young's Modulus in a radial direction AFAM scan from the center to the peripheral of a NP3 fiber in the north direction.

The uniformity of the fiber cross section is even more pronounced in the north direction with smaller variance seen in the average value or the range of values. Calculated Young's modulus values varied from 102.3 ± 11.6 to 102.4 ± 11.6. A similar phenomenon is seen in the south directional scan with the average Young's modulus values differing by 0.5 MPa from the scan closest to the center and the peripheral scan.

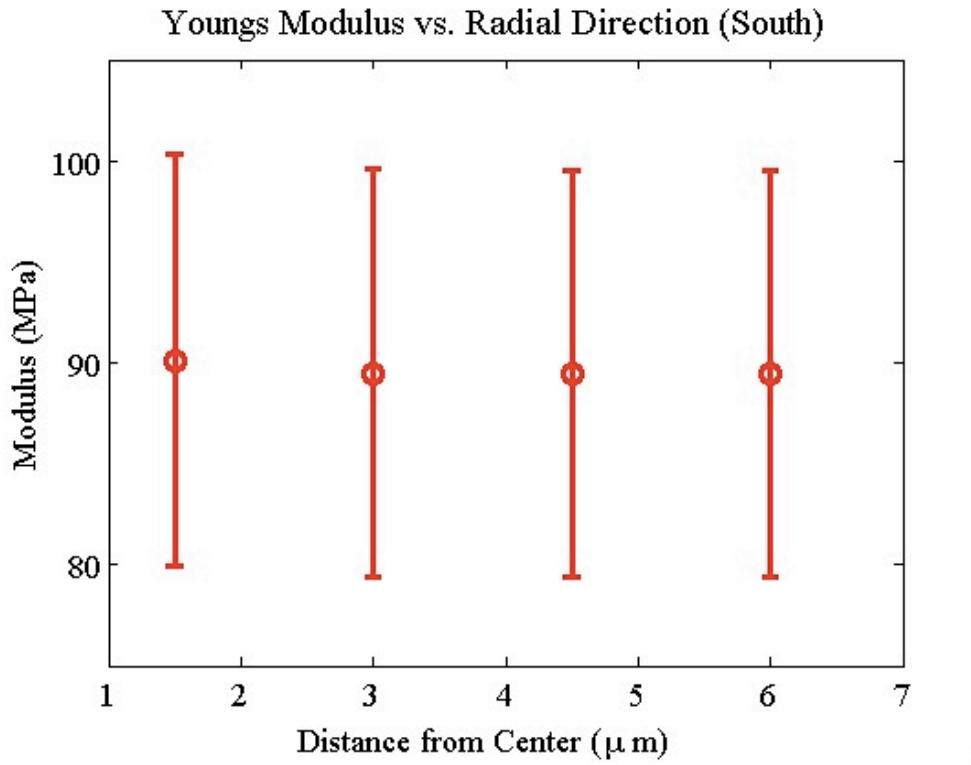

Figure 25 Results of AFAM Young's modulus measurements of a NP3 fiber in the south radial direction. The Young's modulus results vary from 89.4 ± 10.1 MPa to 90.1 ± 10.2 MPa.

Comparing Figure 24 and Figure 25, indicated the Young's modulus values for this particular NP3 fiber is uniform in all directions. The difference in average values between the highest calculated value, 102.3 ± 11.6, and the lowest reported value, 86.7 ± 9.8 MPa, differs by approximately 15 percent. However the large error variance associated with the calculation is almost as large with an average 10 percent error variance seen in most scans. Most of this error variance is a result of how the values are calculated. The AFAM technique requires many assumptions, such a tip geometry, in order to model the tip-sample interaction. For these experiments, the tip radius was measured imaging the used tip under an SEM microscope with approximately 20 percent error seen in radius measurement due to the instrument limitation as well as the 3D nature of the object. The large variation is the main influencing factor on the large

error variance in the calculated Young's modulus values seen in these experiments. In order to calculate the Young's modulus using the AFAM method, the tip is assumed to be a sphere. When measuring the tip radius using the SEM, a spherical shape is imposed over the tip end in order to model the often non-hemispherical tip as a hemisphere. This approach of measuring the tip radius can be different from the actual tip-sample area interaction[69]. Kopycinska-Muller *et al.* measured the tip radii of their cantilevers used in their experiments and found the tip radius can often influence the measurement values by approximately 25 percent for the same sample.

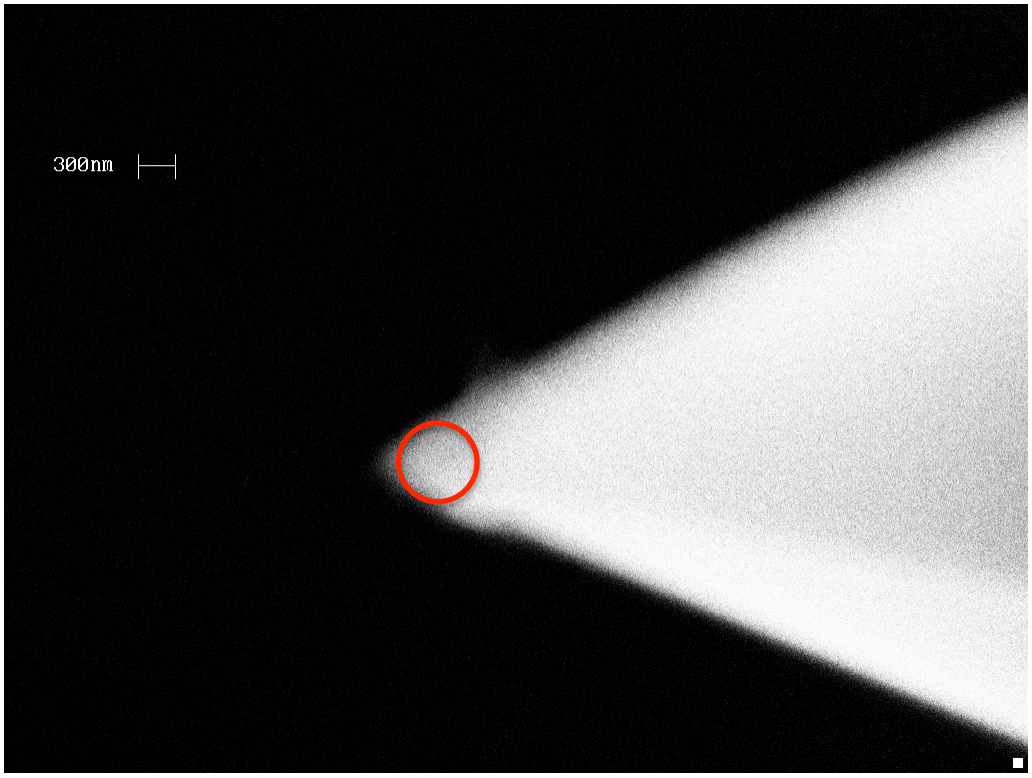

Figure 26 SEM image of a CSG10 tip after an AFAM scan. In order to get the area of tip-sample interaction to be used in AFAM calculation, the tip radius is measured by imposing a hemispherical shape over the end of the tip to best model the spherical interaction assumed by the AFAM theory.

The results of the AFAM Young's modulus of other NP3 fibers reveal a similar uniformity of the Young's modulus across the cross section of the fiber (Figure 27). However the values seen in this second fiber are not as uniform as seen in the previously

discussed fiber. In the East direction there is an 8 percent decrease in the Young's modulus from the center most scan to the peripheral fiber scan. This 8% decrease still lies within the range of error associated with these AFAM measurements. The scan in the West direction, however, shows something not seen in other scans, a drop in modulus of approximately 23 percent three-fourths of the way across the fiber cross section.

This variation may be caused by manufacturing steps out of our control, however it is important to note that traditional mechanical testing methods would not have been able to detect the drop in Young's modulus seen in Figure 27b. A significant advantage of the AFAM technique is its ability to detect differences in material properties at the nanoscale.

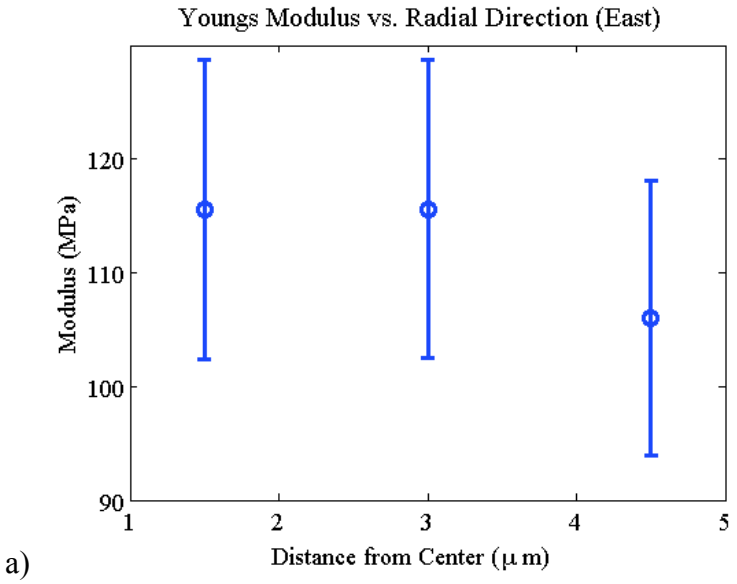

a)

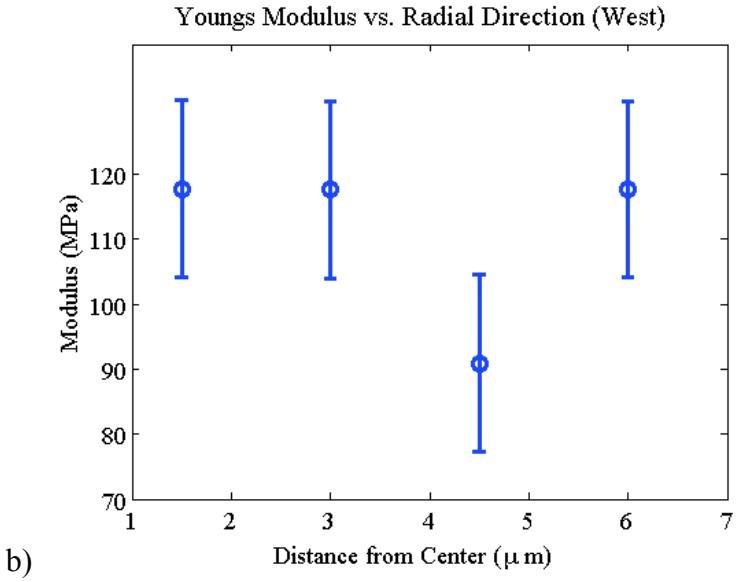

b)

Figure 27 Results of AFAM Young's modulus measurements of a NP3 fiber in the east and west radial direction.

5. Conclusion

The results of this work show changing cantilevers between AFAM scans can have an effect on the calculated Young's modulus of the sample. Scans done on the same material using three separate cantilevers showed a thirty percent difference in calculated Young's modulus. On

the other hand, scans done on the same sample without changing the cantilever resulted in less than a ten percent difference between the Young's modulus values. This suggests that the issue of tip wear may not be a significant factor in AFAM Young's modulus calculations.

Using the same tip to scan each radial direction, results showed the cross section of the bi-component nylon/PET fiber was fairly uniform. Most scans showed only a slight variation in the radial direction but the variations were not statistically significant. The variation in domain sizes within the bi-component fibers does not seem to have a significant impact on the Young's modulus as originally hypothesized. Though most radial scans showed no variation, there were a few scans that showed a decrease in the modulus towards the peripheral of the fiber. This slight decrease in the modulus would not have been seen on traditional tensile strength testing.

Over the course of this work, we have been able to show that the AFAM technique is a viable method to measure the Young's modulus of soft materials such as fibers. This method could then offer a new way to measure the sample properties at the nanoscale without damaging the fiber. New techniques that deliver material properties at the nanoscale will allow future researcher better opportunities understand their samples, not only at the traditional microscale but also at the nanoscale.

6. Recommendations for Future Studies

For future studies, the next logical stop would be to compare the values calculated to values calculated for the exact same fibers using other methods of mechanical testing. The tip-sample interaction is most commonly modeled as a spring even though there maybe much more complicated interactions taking place. There are assumptions about tip shape and contact area that may not be truly representative of the actual system. Other researchers have commonly

compared the nanoindentation and AFAM methods on the same material to judge its validity. Some have seen good agreement between the techniques while others have seen both under and over estimations when comparing the two techniques. Doing a similar comparison for the island-in-the-sea would allow us to see how the AFAM agreement with nanoindentation relates to previous literature. Though the use of nanoindentation on nanofibers is still a very small area of study, a few researchers have been successfully able to use the technique to measure the elastic modulus of the longitudinal axis of fibers. Due to the configuration and preparation of the fibers in this study, it would be possible to measure the latitudinal elastic modulus, further adding to the study of nanoindentation characterized nano fibers.

Another study could be analyzing how the characterization of the cantilever tip changes the recorded elastic modulus. In my study, I choose to measure the radius of curvature for the tip using the SEM. It is hypothesized that variations between tips at the beginning of the experiment is the reason there was such variation between measurements when cantilevers were changed. However since we didn't image the tips at the beginning of the experiment this hypothesis was not tested here. A future study would involve measuring the tip radius before and after each AFAM scan. Knowing exactly how much the tip radius is varying for each scan will enable us to have a better understanding of how the degree of tip radius variation is related to the variations seen in Young's modulus.

7. Appendix A

A.1 Code Used to Calculate Young's Modulus

```
function [Es, stEs] = effectiveModulus(length1,width, height, radius, force, fname)
%Calculate effective modulus and sample modulus
% force in newtons

Ei=169000000000; %Young's Modulus of silicon in Pa
contactstiffness = cantileverconstant(length1, width, height, Ei, fname);
Estar = sqrt((contactstiffness.^3)/(6*radius*force));
stKc = stdspringconstant (length1, width, height, Ei);
sdR = radius*.20; sdF= force*.10;
diffKc = contactstiffness.^2./(4*force*radius*(contactstiffness.^3/(6*force*radius)).^(1/2));
size(diffKc);
diffR = -contactstiffness.^3./(12*force*radius^2*(contactstiffness.^3/(6*force*radius)).^(1/2));
size(diffR);
diffF = -contactstiffness.^3./(12*force^2*radius*(contactstiffness.^3/(6*force*radius)).^(1/2));
size(diffF);
stEstar = sqrt((diffKc.^2*stKc^2)+(diffR.^2*sdR^2)+(diffF.^2*sdF^2));
Et = Ei; %Young's Modulus of silicon
vt = 0.33; %Poisson ratio of silicon
vs = 0.25; %Poisson ratio of nylon

Es = ((Estar*Et*(1-vs^2))./((Et-Estar)-(Estar*(vt^2))))/1000000; %Young Modulus of Sample in
MPa
stEs = (((Et*(vs^2 - 1))./(Estar*vt^2 + Estar - Et) - (Estar*Et*(vs^2 - 1)*(vt^2 + 1))./(Estar*vt^2
+ Estar - Et).^2).*stEstar)/1000000;


%%%
```

```
(((Kc/3)*(KnTimesLen.^3)).*(1+(cos(KnTimesLen).*cosh(KnTimesLen)))./...
   (sinh(KnTimesLen).*cos(KnTimesLen)-(cosh(KnTimesLen).*sin(KnTimesLen)));
size(contactstiffness);

%%%%%%%%%%%%%%%%%%%%%%%%%%%%%%%%%%%%%%%%%%%%%%%%%%%%%%%%%%%%%%%%%%%%%%%%%%%%%%%%
function Kc = springconstant(length1, width, height, Ei)
% length1, width, height in micrometers
Kc = (Ei*(height^3)*width)/(4*(length1^3));


function stKc = stdspringconstant (length1, width, height, Ei)
diffW = (Ei*(height^3))/(4*(length1^3));
diffT = (3*Ei*(height^2)*width)/(4*(length1^3));
diffL = (-3*Ei*(height^3)*width)/(4*(length1^4));
sdW = width*0.025; sdT = height*0.050; sdL = length1*0.025;
stKc = sqrt((diffW^2*sdW^2)+(diffT^2*sdT^2)+(diffL^2*sdL^2));
```

8. References

1. Binnig, G., Gerber, C., and Quate, C. F., "Atomic force microscope" *Phys. Rev. Lett.*, Vol. 56,no. 9, pp. 930-933, 1986.
2. Wiesendanger, R. (1998). *Scanning probe microscopy: Analytical methods*. Berlin: Springer-
2. Wiesendanger, R. (1998). *Scanning probe microscopy: Analytical methods*. Berlin: Springer-
3. Auernhammer, G. K., Butt, H.-J., & Vollmer, D. (2008). *Surface and interfacial forces: From*
3. Auernhammer, G. K., Butt, H.-J., & Vollmer, D. (2008). *Surface and interfacial forces: From fundamentals to applications*. Berlin: Springer-Verlag.
4. Braga, P. C., & Ricci, D. (2004). Atomic force microscopy: Biomedical methods and applications. Totowa, N.J: Humana Press.
5. Asif, S. A., Wahl, K. J., Colton, R. J., Warren, O. L., & Florida Univ Gainesville Dept Of Materials Science And Engineering. (2001). *Quantitative Imaging of Nanoscale Mechanical Properties Using Hybrid Nanoindentation and Force Modulation*. Ft. Belvoir: Defense Technical Information Center.
6. Kumar, C. S. S. R. (2006). Nanosystem characterization tools in the life sciences. Weinheim: Wiley-VCH.
7. Mode, N. "Force Modulation Microscopy (FMM)." Force Amplitude and Phase Imaging of Sample Elasticity. ParkAFM. 11 November 2011 <http://www.nanowerk.com/nanobusiness/showroom/Park_Systems/downloads/Force_Modulation_Microscopy.pdf>.
8. Rabe, U., & Arnold, W. (January 01, 1994). Acoustic microscopy by atomic force microscopy. *Applied Physics Letters, 64,* 12, 1493.
9. Rabe, U., Amelio, S., Kester, E., Scherer, V., Hirsekorn, S., & Arnold, W. (January 01, 2000). Quantitative determination of contact stiffness using atomic force acoustic microscopy. *Ultrasonics, 38,* 1, 430.
10. Mangamma, G., Dash, S., Tyagi, A. K., Raj, B., Kant, M., & Rao, M. S. R. (June 01, 2009). Atomic Force Acoustic Microscopy of nanostructured SiC coatings. *Journal of Scanning Probe Microscopy, 4,* 1, 36-41.
11. Marinello, F., Savio, E., Schiavuta, P., Vezzu, S., Patelli, A., & Carmignato, S. (June 03, 2011). Atomic force acoustic microscopy for quantitative nanomechanical characterization. Wear, 271, 534-538.
12. Meirovitch, L. (1986). Elements of vibration analysis. New York: McGraw-Hill.
13. Rabe, U., Janser, K., & Arnold, W. (January 01, 1996). Vibrations of free and surface-coupled atomic force microscope cantilevers: Theory and experiment. *Review of Scientific Instruments, 67,* 9, 3281-3293.
14. Wright, O. B., & Nishiguc, N. (August 04, 1997). Vibrational dynamics of force microscopy: Effect of tip dimensions. *Applied Physics Letters, 71,* 5, 626-628.
15. Volterra, E., & Zachmanoglou, E. C. (1965). Dynamics of vibrations. Columbus, Ohio: C.E. Merrill Books.
16. Atkins, P. W. (1978). Physical chemistry. San Francisco: W.H. Freeman.
17. Greenberg, M. D. (1998). Advanced engineering mathematics. Upper Saddle River, N.J: Prentice Hall.
18. Bottega, W. J. (2006). *Engineering vibrations*. Boca Raton: CRC/Taylor & Francis.
19. Zhao, M. H., Ye, Z. Z., & Mao, S. X. (January 01, 2009). Photoinduced stiffening in ZnO nanobelts. Physical Review Letters, 102, 4.)

20. Timoshenko, S., & Goodier, J. N. (1970). Theory of elasticity. New York: McGraw-Hill.
21. Turner, J. A., & Wiehn, J. S. (January 01, 2001). Sensitivity of flexural and torsional vibration modes of atomic force microscope cantilevers to surface stiffness variations. *Nanotechnology, 12,* 322-330.
22. Johnson, K. L. (1985). *Contact mechanics*. Cambridge [Cambridgeshire: Cambridge University Press.
23. Gohar, R. (1988). *Elastohydrodynamics*. Chichester, West Sussex: E. Horwood.
24. Kim, J. H., Balogun, O., & Shah, S. P. (December 01, 2010). Atomic Force Acoustic Microscopy to Measure Nanoscale Mechanical Properties of Cement Pastes. *Transportation Research Record: Journal of the Transportation Research Board*, 2141, -1, 102-108.
25. Marinello, F., Schiavuta, P., Carmignato, S., & Savio, E. (January 01, 2010). Critical factors in quantitative Atomic Force Acoustic Microscopy. *Cirp Journal of Manufacturing Science and Technology*, 3, 1, 49-54.
26. Rabe, U., Kopycinska, M., Hirsekorn, S., Saldana, J. M., Schneider, G. A., & Arnold, W. (October 21, 2002). High-resolution characterization of piezoelectric ceramics by ultrasonic scanning force microscopy techniques. *Journal of Physics. D: Applied Physics, 35,* 2621-2635.
27. Bechmann, R., Landolt, H., Börnstein, R., Hearmon, R. F. S., & Hellwege, K. H. (1966). *Landolt-Börnstein: Numerical data and functional relationships in science and technology*. Berlin: Springer-Verlag.
28. Schaefer, A., Schmitt, H., & Dörr, A. (July 01, 1986). Elastic and piezoelectric coefficients of TSSG barium titanate single crystals. *Ferroelectrics, 69,* 253-266.
29. Hurley, D. C., Shen, K., Jennett, N. M., & Turner, J. A. (January 01, 2003). Atomic force acoustic microscopy methods to determine thin-film elastic properties. *Journal of Applied Physics, 94,* 4, 2347.
30. Kopycinska-Müller, M., Geiss, R. H., Müller, J., & Hurley, D. C. (June 01, 2005). Elastic-property measurements of ultrathin films using atomic force acoustic microscopy. *Nanotechnology, 16,* 6, 703-709.
31. Passeri, D., Rossi, M., Alippi, A., Bettucci, A., Manno, D., Serra, A., Filippo, E., ... Davoli, I. (October 01, 2008). Atomic force acoustic microscopy characterization of nanostructured selenium–tin thin films. *Superlattices and Microstructures, 44,* 641-649.
32. Mege, F., Volpi, F., & Verdier, M. (March 01, 2010). Mapping of elastic modulus at sub-micrometer scale with acoustic contact resonance AFM. *Microelectronic Engineering, 87,* 3, 416-420.
33. Kassavetis, S. N., Logothetidis, S., & Matenoglou, G. M. (January 01, 2006). Near-surface mechanical properties and surface morphology of hydrogenated amorphous carbon thin films. *Surface & Coatings Technology, 200,* 22, 6400.
34. Stan, G. P. W. (January 01, 2006). Quantitative measurements of indentation moduli by atomic force acoustic microscopy using a dual reference method. *Review of Scientific Instruments, 77,* 10, 103707.
35. Banerjee, S., Gayathri, N., Shannigrahi, S. R., Dash, S., Tyagi, A. K., & Raj, B. (April 21, 2007). Imaging distribution of local stiffness over surfaces using atomic force acoustic microscopy. *Journal of Physics. D, Applied Physics, 40,* 8, 2539-2547.

36. Luo, H. S., & Yin, Q. R. (January 01, 2005). Local elasticity imaging of ferroelectric domains in Pb(Mg1/3Nb2/3)O3-PbTiO3 single crystals by low-frequency atomic force acoustic microscopy. *Solid State Communications, 133*, 8, 521-525.
37. Karagiannidis, P. G., Kassavetis, S., Pitsalidis, C., Logothetidis, S., & Carbon- or Nitrogen-Containing Nanostructured Composite Films. (April 01, 2011). Thermal annealing effect on the nanomechanical properties and structure of P3HT:PCBM thin films. *Thin Solid Films, 519,* 12, 4105-4109.
38. Kumar, A., Rabe, U., & Arnold, W. (January 01, 2008). Mapping of Elastic Stiffness in an alpha + beta Titanium Alloy using Atomic Force Acoustic Microscopy. *Japanese Journal of Applied Physics New Series-, 47,* 7, 6077-6080.
39. Lee, Y. T., & Welsch, G. (August 01, 1990). Young's modulus and damping of Ti-6Al-4V alloy as a function of heat treatment and oxygen concentration. *Materials Science and Engineering, A: Structural Materials: Properties, Microstructure and Processing,* 77-89.
40. Leyens, C., & Peters, M. (2003). Titanium and titanium alloys: Fundamentals and applications. Weinheim: Wiley-VCH.
41. Simmons, G., & Wang, H. (1971). Single crystal elastic constants and calculated aggregate properties: A handbook. Cambridge, Mass: M.I.T. Press.
42. Stehlik, S., Knotek, P., Wagner, T., Zima, V., Bartos, M., Kasap, S. O., & Frumar, M. (January 01, 2009). Study of microstructure in Agx(As0.33Se0.67)100-x chalcogenide glasses. *Journal of Noncrystalline Solids, 355,* 2054-2058.
43. Zhao, K.-Y., Zeng, H.-R., Song, H.-Z., Hui, S.-X., Li, G.-R., Yin, Q.-R., Shimamura, K., ... Kitamura, K. (September 01, 2008). Acoustic imaging frequency dynamics of ferroelectric domains by atomic force microscopy. *Chinese Physics Letters, 25,* 9, 3429-3432.
44. Mangamma, G., Dash, S., Tyagi, A. K., Raj, B., Kant, M., & Rao, M. S. R. (June 01, 2009). Atomic Force Acoustic Microscopy of nanostructured SiC coatings. Journal of Scanning Probe Microscopy, 4, 1, 36-41.
45. Lee, H. G., Kang, T. W., Hong, S. U., Paek, M. C., & Kim, T. W. (January 01, 2001). Crystallization of 3C-SiC (111) Thin Films Grown on Si (111) Substrates by Post Thermal Annealing. *Japanese Journal of Applied Physics Part 1 Regular Papers Short Notes and Review Papers, 40,* 548, 6304-6306
46. Chen, J., Scofield, J., & Steckl, A. J. (January 01, 2000). Formation of SiC SOI Structures by Direct Growth on Insulating Layers. *Journal of the Electrochemical Society, 147,* 10.)
47. He, C.-F., Zhang, G.-M., & Wu, B. (August 01, 2010). Quantitative measurement of local elasticity of SiOx film by atomic force acoustic microscopy. *Chinese Physics B, 19,* 8.)
48. Prasad, M. (January 01, 2002). Measurement of Young's modulus of clay minerals using atomic force acoustic microscopy. *Geophysical Research Letters, 29,* 8.)
49. Kopycinska-Muller, M., Prasad, M., Rabe, U., & Arnold, W. (January 01, 2007). Elastic Properties of Clay Minerals Determined by Atomic Force Acoustic Microscopy Technique. *Acoustical Imaging : [proceedings of the ... International Symposium on Acoustical Imaging], 28,* 409-416.
50. Berge, P. A., & Berryman, J. G. (January 01, 1995). Realizability of Negative Pore Compressibility in Poroelastic Composites. *Transactions- American Society of Mechanical Engineers Journal of Applied Mechanics, 62,* 4, 1053-1062.

51. Hurley, D. C., Kopycinska-Muller, M., Kos, A. B., & Geiss, R. H. (January 01, 2005). Quantitative Elastic-Property Measurements at the Nanoscale with Atomic Force Acoustic Microscopy. *Advanced Engineering Materials, 7,* 8, 713-718.
52. Kos, A. B., & Hurley, D. C. (February 07, 2008). Nanomechanical mapping with resonance tracking scanned probe microscope. *Measurement Science and Technology, 19,* 1.)
53. Passeri, D., Rossi, M., Alippi, A., Bettucci, A., Terranova, M. L., Tamburri, E., & Toschi, F. (May 01, 2008). Characterization of epoxy/single-walled carbon nanotubes composite samples via atomic force acoustic microscopy. *Physica E: Low-Dimensional Systems and Nanostructures, 40,* 7, 2419-2424.
54. Karagiannidis, P. G., Kassavetis, S., Pitsalidis, C., Logothetidis, S., (April 01, 2011). Thermal annealing effect on the nanomechanical properties and structure of P3HT:PCBM thin films. *Thin Solid Films, 519,* 12, 4105-4109.
55. Preghenella, M., Pegoretti, A., & Migliaresi, C. (2006). Atomic force acoustic microscopy analysis of epoxy–silica nanocomposites. *Polymer Testing*, 25(4), 443-451.
56. Zhao, W., Korach, C. S., & Singh, R. P. (May 01, 2009). Effects of environmental degradation on near-fiber nanomechanical properties of carbon fiber epoxy composites. *Composites Part A: Applied Science and Manufacturing, 40,* 5, 675-678.
57. Liu, Y., Chen, S., Rafailovich, M., Zussman, E., Korach, C. S., & Zhao, W. (June 14, 2011). Diameter-dependent modulus and melting behavior in electrospun semicrystalline polymer fibers. *Macromolecules, 44,* 11, 4439-4444.
58. Geiss, R., Hurley, D., Kopycinska-Mueller, M., & Rice, P. (January 01, 2004). Influence of Tip Wear on Atomic Force Acoustic Microscopy Experiments. *Materials Research Society Symposia Proceedings*, 838, 146-151.
59. Amelio, S., Goldade, A. V., Rabe, U., Scherer, V., Bhushan, B., & Arnold, W. (January 01, 2001). Measurements of elastic properties of ultra-thin diamond-like carbon coatings using atomic force acoustic microscopy. *Thin Solid Films*, 392, 1, 75-84.
60. Geiss, R. H., Kopycinska-Muller, M., & Hurley, D. C. (January 01, 2005). Wear of Si Cantilever Tips used in Atomic Force Acoustic Microscopy. Microscopy and Microanalysis New York-, 11.
61. Zhao, W., Korach, C. S., & ASME 2009 International Mechanical Engineering Congress and Exposition, IMECE2009. (July 09, 2010). Measurement of epoxy stiffness by atomic force acoustic microscopy. *Asme International Mechanical Engineering Congress and Exposition, Proceedings, 12,* 85-87.
62. Dugan J.; Homonoff, E.; Synthetic Split Microfiber Technology for Filtration, Retrieved at http://www.fitfibers.com/files/Microfibers%20for%20Filtration.docon 04/20/2012
63. Lewin, M. (1996). Handbook of fiber science and technology: 3,4. New York u.a: Dekker
64. Mbwana Suleiman Ndaro, Xiang-yu Jin, Ph.D, Ting Chen, Ph.D., & Chong-wen Yu, Ph.D. (2007). *Splitting of Islands-in-the-Sea Fibers (PA6/COPET) During Hydroentangling of Nonwovens*. INDA, Association of the Nonwovens Fabrics Industry.
65. Nakajima, T., Kajiwara, K., & McIntyre, J. E. (1994). Advanced fiber spinning technology. Cambridge, England: Woodhead.
66. Y. Moriki, M. Ogasawara. Spinneret for production of composite filaments. US Patent 4445833, May 1, 1984
67. T. Kiriyama, S. Norota, Y. Segawa, S. Emi, T. Imoto, T. Azumi. Novel assembly of composite fibers. US Patent 4414276 , November 8, 1983

68. W. H. Hills. Method of making plural component fibers. US Patent 5162074, November 10, 1992
69. Kopycinska-Muller, M., Geiss, R. H., & Hurley, D. C. (April 01, 2006). Contact mechanics and tip shape in AFM-based nanomechanical measurements. *Ultramicroscopy*, 106, 6, 466-474.
70. Khurshudov, A., & Kato, K. (January 01, 1995). Wear of the atomic force microscope tip under light load, studied by atomic force microscopy. *Ultramicroscopy*, 60, 1, 11.
71. Bloo, M. L., Haitjema, H., & Pril, W. O. (January 01, 1999). Deformation and wear of pyramidal, silicon-nitride AFM tips scanning micrometre-size features in contact mode. *Measurement: Journal of the International Measurement Confederation*, 25, 3, 203.